Research Summary No. 36-7, Volume II

for the period December 1, 1960 to February 1, 1961

(NASA Contract NASw-6)

;JPL-RS.-36-7, Vol.2)

jpl

JET PROPULSION LABORATORY
CALIFORNIA INSTITUTE OF TECHNOLOGY
PASADENA, CALIFORNIA

March 1, 1961

Research Summary No. 36-7, Volume II

for the period December 1, 1960 to February 1, 1961

JET PROPULSION LABORATORY

CALIFORNIA INSTITUTE OF TECHNOLOGY

PASADENA, CALIFORNIA

March 1, 1961

Preface

The *Research Summary* is a bimonthly report of supporting research and development conducted at the Jet Propulsion Laboratory.

This periodical is issued in three volumes. Volume I contains summaries of the work accomplished by the Space Sciences, Systems, Guidance and Control, and Telecommunications Divisions of the Laboratory. Volume II contains summaries of the work accomplished by the Physical Sciences, Engineering Mechanics, Engineering Facilities, and Propulsion Divisions. All work of a classified nature is contained in Volume III.

W. H. Pickering, *Director*
Jet Propulsion Laboratory

Research Summary No. 36-7

Volume II

Contents

PHYSICAL SCIENCES DIVISION

I. Physics Research

A. Upper Atmosphere Physics, Mars

The results of the extensive computer calculations that have been made of the nitrogen and oxygen atomic reactions in the upper atmosphere of the Earth (Research Summary Nos. 36-5, 36-6, Ref 1) have now been applied to the atmosphere of Mars. In terms of the physics of their upper atmospheres, the most important differences between Mars and the Earth are caused by the weaker Martian gravitational field and the smaller amount of molecular oxygen in its atmosphere.

The upper atmosphere density curve of the Earth, which is the result of numerous rocket and satellite measurements, was used as a model upper atmosphere for Mars by calculating equivalent heights for equal densities in the two upper atmospheres. The hydrostatic equation for an isothermal atmosphere was used in these calculations.

$$n = n_0 e^{-h/H} \qquad (1)$$

$$H = \frac{kT}{mg} \qquad (2)$$

The particle density is indicated by n and the density at ground level by n_0; h is the height above ground level and H the scale height; kT is the kinetic energy of the atmospheric gas and mg the gravitational force on the gas. Since the surface gravity on Mars is about 0.4 times the surface gravity of the Earth (Ref 2), the scale height of Mars is about 2.5 times that of the Earth. The equivalent heights were calculated from Equation (1) using a Martian surface atmospheric density equal to one-twelfth the value for the Earth. The variation of atmospheric density with height as it applies to the two planets is shown in Figure 1a. The density when referred to the ordinate scale on the right of the figure pertains to Earth; the density when referred to the height scale on the left pertains to Mars.

In an isothermal or constant scale height-gradient atmosphere, the rate of absorption of radiation of a particular wavelength and, hence, the rate of atom production is given by the following expression

$$q = \sigma n I_0 e^{-\sigma n H} \qquad (3)$$

where q is the atom production rate, n the density of the molecule that is being dissociated, I_0 the solar radiation incident at the top of the atmosphere, and H the scale height. The maximum rate of dissociation occurs at a level where the exponent in Equation (3) is equal to one.

$$\sigma n H = 1 \qquad (4)$$

The maximum rate of dissociation is then

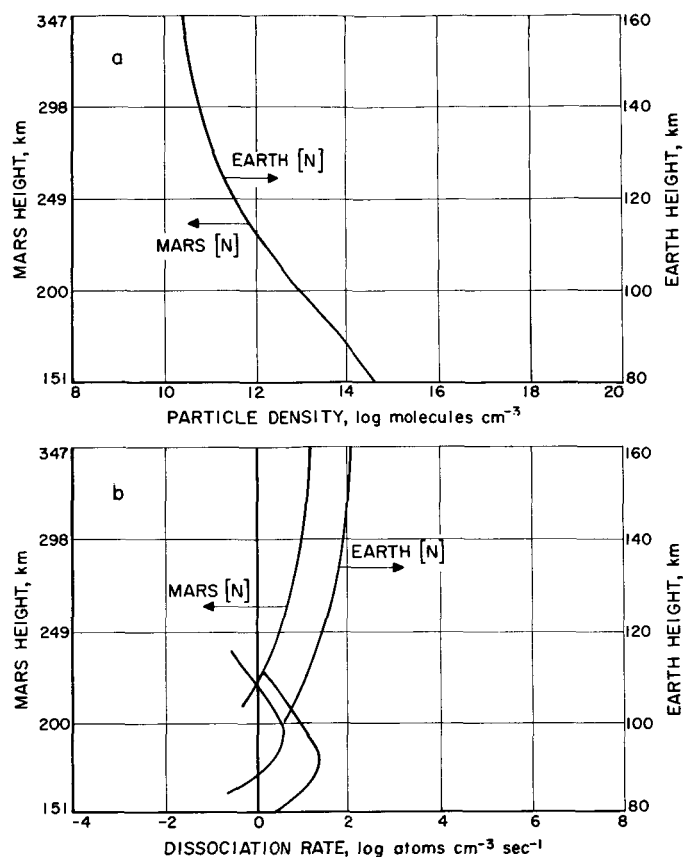$$q_{max} = \sigma n I_0 e^{-1} = \frac{I_0}{eH} \qquad (5)$$

Figure 1. Comparison of density and rate of molecular nitrogen dissociation in upper atmospheres of Earth and Mars

Table 1. Atmospheric conversion factors

Parameter	Earth	Mars
Scale height	H_E	$2.5\,H_E$
Solar intensity	I_E	$0.5\,I_E$
Atmospheric density at ground level	n_E	$n_E/12$
Maximum rate of absorption	q_E	$0.2\,q_E$
Atmospheric density at maximum absorption	n_m	$0.4\,n_m$

taken from Reference 1. These dissociation curves are made applicable to the Martian atmosphere by the use of the quantities in Table 1. The dissociation curves are transposed to the left because of the smaller maximum absorption rate and are transposed upward because of the lower density where maximum absorption occurs. The vertical scale on the left gives the heights for the curves pertaining to the Martian atmosphere, while the scale on the right is used for Earth's atmosphere.

In contrast to Earth's atmosphere which contains about 20% molecular oxygen, the Martian atmosphere may contain only 0.1% oxygen (Ref 2). In analogy to the Earth, most of the remainder of the Martian atmosphere is assumed to be molecular nitrogen. The results of the atom reaction calculations in Reference 1 were applied to a model Martian atmosphere containing 0.1% O_2, 99.9% N_2 by the use of the conversion factors in Table 1. The resulting atom densities are plotted in Figure 2. The symbols N, O, and M in brackets denote the nitrogen atom, oxygen atom, and total particle densities, respectively. The 100-km level in Earth's atmosphere has an equivalent density to the 200-km level of the Martian atmosphere (Fig 1a). At this level, the Martian atmosphere

Hence, the magnitude of the atom production in a planetary atmosphere is determined only by the intensity of the incident radiation and the scale height of the atmosphere. Since the orbit distance of Mars from the Sun is about 1.4 times the distance of the Earth from the Sun, the intensity of the solar radiation incident upon the Martian upper atmosphere is about one-half the intensity above Earth's atmosphere. Using the ratio of solar intensities and scale heights and Equation (5), the maximum rate of absorption of a particular wavelength in the Martian atmosphere is found to be 0.2 times the rate of absorption in Earth's atmosphere.

The atmospheric density, at which the maximum rate of absorption occurs, may be calculated from Equation (4). The density in the Martian atmosphere is inversely proportional to the ratio of scale heights or 0.4 times the density at maximum absorption in Earth's atmosphere.

All of these physical properties of the two atmospheres are summarized in Table 1. In Figure 1b, the rate of dissociation of molecular nitrogen in Earth's atmosphere is
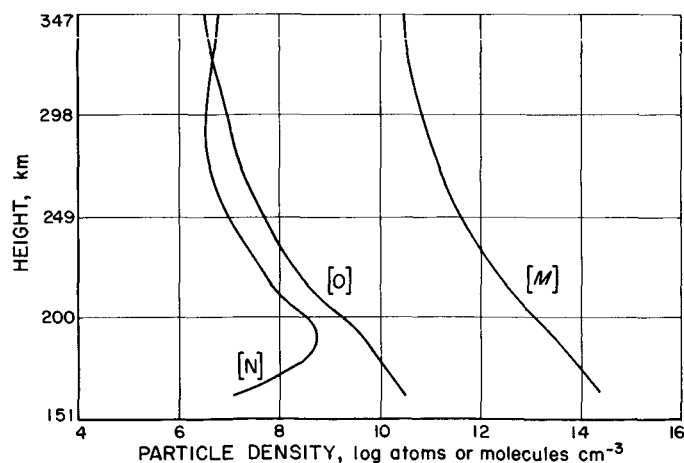
Figure 2. Nitrogen and oxygen atom densities in model Martian atmosphere containing 0.1% O_2 and 99.9% N_2

has about 2.5 orders of magnitude less atomic oxygen than the Earth does at the equivalent height, while it has about 2.5 orders of magnitude more atomic nitrogen than the Earth at the comparable level. The atom densities in Earth's atmosphere are plotted in Figure 3.

Since the relative nitrogen–oxygen atom densities in the Martian atmosphere are different than the relative atom densities in Earth's atmosphere, the spectrum of the night airglow of Mars will be much different from the spectrum of Earth's airglow. The molecular oxygen spectra of the Herzberg and atmospheric bands in the ultraviolet and infrared are the dominant molecular emissions of Earth's airglow since the density of atomic oxygen far exceeds the atomic nitrogen density. In the Martian atmosphere, however, since the atomic oxygen density is nearly equal to the atomic nitrogen, the most intense feature of the atomic recombination airglow should be the beta bands of nitric oxide in the blue and ultraviolet portion of the spectrum. (See *Research Summary 36-3* for laboratory measurements of this airglow.)
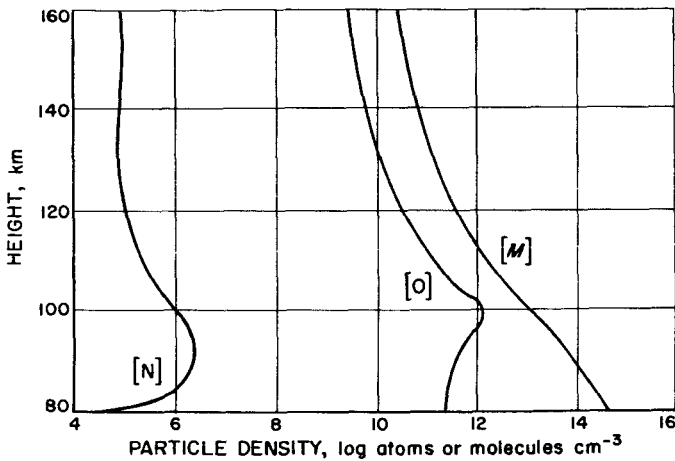

Figure 3. Nitrogen and oxygen atom densities in Earth's atmosphere

B. Exact Solutions of Transport Equation in Spherical Geometry

The one-velocity time-independent linear Boltzmann equation for neutron transport with no sources and spherically symmetric scattering reduces in the case of spherical symmetry to

$$\mu \frac{\partial F}{\partial r} + \frac{1 - \mu^2}{r} \frac{\partial F}{\partial \mu} + F = c\phi \tag{1}$$

Here $F(r, \mu)$ is the neutron angular distribution function: the number of neutrons at r in a unit solid angle about the direction $\vec{\Omega}$, passing through a unit cross section perpendicular to $\vec{\Omega}$ in 1 second; μ is the cosine of the angle between $\vec{\Omega}$ and the radius vector $\vec{r}$, and so $-1 \leq \mu \leq 1$; r is measured in mean-free-paths $\lambda = \Sigma_t^{-1}$, and the scattering and absorbing medium in which the transport occurs is homogeneous; $\Sigma_t = \Sigma_a + \Sigma_s$ where Σ_a is the macroscopic absorption cross section of the medium, and where Σ_s is the macroscopic scattering cross section of the medium; $c = \Sigma_s/\Sigma_t$. If $\Sigma_a < 0$, i.e., if $c > 1$, the medium is multiplying, and one is dealing with a monoenergetic model of a homogeneous chain reactor.

Equation (1) is integro-differential, inasmuch as the collision integral or neutron flux ϕ is given by

$$\phi = \frac{1}{2} \int_{-1}^{1} F \, d\mu \tag{2}$$

Physically, ϕ is the density of neutrons, multiplied by the scalar speed of the neutrons.

A recent paper by Case (Ref 3) has investigated the orthogonality and completeness properties of a family of singular solutions of the same problem, in the case of plane symmetry.

It has been found recently that there are similar exact solutions to Equation (1). These are best written in the form

$$F_\nu (r, \mu) = \sum_{n=0}^{\infty} (-1)^n (n + \tfrac{1}{2}) i_n (r/\nu) p_n (\nu) P_n (\mu) \tag{3}$$

where the i_n is a spherical Bessel function:

$$i_n (z) = \sqrt{\frac{2\pi}{z}} I_{n+\frac{1}{2}} (z) \tag{4}$$

$I_{n+\frac{1}{2}}(z)$ is a modified Bessel function of half-integral order. The recurrence relations for the i_n are

$$i_{n-1} - i_{n+1} = \frac{2n + 1}{z} i_n \tag{5}$$

$$i'_n = i_{n\pm 1} \pm \frac{n + \frac{1}{2} \mp \frac{1}{2}}{z} i_n \tag{6}$$

It is noted that

$$i_0 = \frac{2 \sinh z}{z} \tag{7}$$

and for large argument

$$i_n \rightarrow \frac{e^z}{z} \tag{8}$$

$p_n(v)$ is a polynomial of degree n. It is defined by the values

$$p_0(v) = 1$$
$$p_1(v) = v(1 - c) \tag{9}$$

and the recurrence relation

$$n p_{n-1}(v) + (n + 1) p_{n+1}(v) = (2n + 1) v p_n(v) \tag{10}$$

This recurrence relation is, of course, also that of Legendre polynomials $P_n(v)$, but the present restriction to $n \geqq 1$ should be noted. Alternatively, the polynomial $p_n(v)$ is given by

$$p_n(v) = P_n(v) - cv W_{n-1}(v) \tag{11}$$

where $W_{n-1}(v)$ is the polynomial of degree $(n - 1)$ treated by Magnus and Oberhetinger (Ref 4).

Integration of Equation (3) on μ gives

$$\phi_v(r) = \frac{\sinh(r/v)}{r/v} \tag{12}$$

and substitution into Equation (1) then shows that Equation (3) is indeed a solution. It can also be written

$$F_v(r, \mu) = \lambda(v) g(r/v, \mu, v) + \frac{cv}{2} P \int_{-1}^{1} \frac{g(r/v, \mu, t)}{v - t} dt \tag{13}$$

where now the $\lambda(v)$ terminology of Case (Ref 3) is introduced and

$$g(z, \mu, v) = \sum_{n=0}^{\infty} (-1)^n \left(n + \tfrac{1}{2}\right) i_n(z) P_n(v) P_n(\mu)$$
$$= I_0 \left(z \sqrt{1 - v^2} \sqrt{1 - \mu^2}\right) e^{-z\mu v} \tag{14}$$

The formal analogy with the plane solutions of Case is obvious. At large values of r, the spherical solutions that have been obtained reduce to the plane solutions with positive v.

The solutions for the spherical case are continuous and not pathological; however, they are not orthogonal. Neither are they complete: note that solutions, which at large r go over to the plane solutions with negative v, have not been found.[a] All the present solutions are even and well-behaved at the origin; all of the present solutions may be called *inside* solutions to suggest that they will occur in situations where a spherically bounded medium is subjected to neutron fluxes from without. Problems of transport in a spherical shell region subjected to neutron fluxes from sources inside as well are not yet able to be treated by superposition methods.

[a] A series of the form of Equation (3), but with the spherical Bessel function $k_n(r/v)$ replacing $(-1)^n i_n(r/v)$, *formally* satisfies the transport Equation (1), and has flux $e^{r/v}/(r/v)$, but unfortunately such a series diverges.

C. Comparison of Fission Electric Cell Geometries

The best over-all criterion for usefulness of a fission cell reactor, or any other reactor in space applications, is probably the ratio of electrical power, output to weight of the entire system, including reactor, radiator, shielding, coolant, piping, and pump. Unfortunately, short of a detailed system design, it is not possible to accurately determine and maximize this ratio with respect to cell geometry. However, if certain assumptions are made about the nature of the reactor and system, a reasonable comparison of power-to-weight ratio for different cell geometries can be achieved.

1. Assumptions

All reactors of the type now being considered for fission electric cell spacecraft power units may be compared if the following assumptions are made for the systems, exclusive of radiation shielding:

(1) The reactors being compared are identical in weight, size, void volume, moderator volume, and fuel loading.

(2) Changes in neutron leakage and velocity spectrum and, therefore, criticality due to different void configurations are ignored.

(3) The weight of components other than reactor and radiator is almost all due to coolant, piping, and pump. Since these will be much smaller in weight than the radiator and will vary with power in a somewhat similar way, they are included in the $(Wt)_{rad}$ below.

(4) Radiator weight is directly proportional to the power being radiated away, which is practically the total reactor power for these low-efficiency systems: $(Wt)_{rad} = \alpha P$.

(5) Reactor weight is directly proportional to moderator volume, the weight of structure and coolant in the core being taken as some constant fraction of the moderator weight, and their volume fractions ignored:

$$(Wt)_{reac} = \beta \times (\text{moderator volume})$$

2. Power-to-Weight Ratio Comparison of Cell Geometries

The cell geometries to be compared are parallel plane, concentric cylinder, and concentric sphere. The calcula-

tions below will be limited to cells consisting of electrode pairs, with fissionable material distributed on the outer surface of the inner electrode in the cylindrical and spherical cases. Under the simplifying assumptions listed above, reactor weights have been forced to equality, but not the electric power output from the reactors. This output is simply (reactor power) $\times$ (efficiency), with the efficiency a function of voltage, fuel layer thickness, and geometry. The reactor power, however, will depend upon conditions of operation. If temperatures and temperature gradients in the moderator are the limiting factor, then it seems reasonable that constant power density, ratio of reactor power to moderator volume (and, therefore, constant total power), be assumed for all geometries. On the other hand, if power is limited by fuel layer temperatures, then total power may well be proportional to fuel area, which is a function of geometry. Both of these possibilities are considered below.

a. Constant power density. In accord with the assumptions listed above (Sec 1), two systems of different cell geometry but identical power density can be compared:

$$\frac{\left(\dfrac{\text{Electric power}}{\text{System weight}}\right)_1}{\left(\dfrac{\text{Electric power}}{\text{System weight}}\right)_2} = \frac{\left(\dfrac{P \times \text{Efficiency}}{\text{System weight}}\right)_1}{\left(\dfrac{P \times \text{Efficiency}}{\text{System weight}}\right)_2} = \frac{(\text{Efficiency})_1}{(\text{Efficiency})_2}$$

Equal void volumes have been assumed for all reactors being compared, the void volume being just the vacuum region between electrodes in the fission cells. For different cell geometries, this constant void volume leads to different fuel surface areas; it follows that the fuel layer thicknesses must also vary with the geometry in order to achieve equal fuel loadings on these different surface areas. The amount of surface area is obtained from the relation:

$$A = \text{Surface area} = (\text{Void volume}) \times \left(\frac{\text{Surface area}}{\text{Void volume}}\right)_{cell}$$

since the void volume of the core is entirely contained in the fission cells. The second factor above is, for the three basic geometries:

$$\left(\frac{\text{Surface area}}{\text{Void volume}}\right)_{pla} = \frac{1}{d}$$

$$\left(\frac{\text{Surface area}}{\text{Void volume}}\right)_{cyl} = \frac{2R_1}{R_2^2 - R_1^2}$$

$$\left(\frac{\text{Surface area}}{\text{Void volume}}\right)_{sph} = \frac{3R_1^2}{R_2^3 - R_1^3}$$

where d is the separation distance between parallel plane electrodes; R_1 and R_2 are the inner and outer electrode

radii, respectively, for concentric cylinders and spheres. The fuel layer has been assumed to be on the outer surface of the inner electrode in the two latter cases. To provide equal fuel loadings in the different reactors, the fuel layer thicknesses, τ, must then be related by:

$$\tau_{pla} = \frac{2R_1 d}{(R_2^2 - R_1^2)} \tau_{cyl} = \frac{3R_1^2 d}{(R_2^3 - R_1^3)} \tau_{sph}$$

In order to utilize these fuel thickness expressions in calculating efficiency ratios, it is necessary to determine the relationship between d, R_1, and R_2 for equivalent reactors of different cell geometries. In addition to the assumptions of equal fuel loadings, void and moderator volumes, and weights indicated above, this equivalence is further defined to mean that the fission cells in the reactors being compared must operate at equal voltages. Since the core of least weight in any geometry is that one which has the smallest void volume, it can be assumed that the electrode separation will always be selected close to the minimum value which will withstand breakdown at operating voltage. Thus, the additional equivalence criterion can be restated as the requirement for achieving the same voltage before breakdown (or significant current leakage) occurs in the different cell geometries. Unfortunately, a good criterion for selecting minimum electrode separations to hold specified voltages is not presently known; and until experiments are actually carried out, it can only be guessed at. However, it is possible to select two extreme cases for present purposes:

(1) Equal separation distances between electrodes in all geometries:

$$R_2 - R_1 = d$$

(2) Equal maximum electric field between electrodes in all cases:

For plane electrodes

$$E_{max} = E_{const} = -\frac{V}{d}$$

For cylindrical electrodes

$$E_{max} = E(R_1) = -\frac{V}{R_1} \frac{1}{\ln (R_2/R_1)}$$

For spherical electrodes

$$E_{max} = E(R_1) = -\frac{V(R_2/R_1)}{R_2 - R_1}$$

$$\therefore \left[\frac{1}{d}\right]_{pla} = \left[\frac{1}{R_1} \frac{1}{\ln (R_2/R_1)}\right]_{cyl} = \left[\frac{R_2/R_1}{(R_2 - R_1)}\right]_{sph}$$

where V is the voltage difference between electrodes.

For any specified void fraction (which determined R_1/R_2), either of the two criteria above will give unique values of R_1 and R_2 for the cylindrical or spherical cell reactor which is equivalent to a reactor containing parallel plate cells of separation distance d.

In obtaining R_1/R_2 from a given void fraction, it is assumed that the cylindrical or spherical cells are in close-packed array in the core. In an infinite array of close-packed elements, the fraction of total volume contained within the cells would be:

$$\left(\frac{\text{Cell volume}}{\text{Total volume}}\right)_{cyl} = 0.908$$

$$\left(\frac{\text{Cell volume}}{\text{Total volume}}\right)_{sph} = 0.739$$

From these, the corresponding expressions for void fraction are obtained:

$$(\text{Void frac}) = \left(\frac{\text{Cell volume}}{\text{Total volume}}\right) \times \left(\frac{\text{Void volume/Cell}}{\text{Cell volume}}\right)$$

$$(\text{Void frac})_{cyl} = 0.908\left(\frac{R_2^2 - R_1^2}{R_2^2}\right)$$

$$(\text{Void frac})_{sph} = 0.739\left(\frac{R_2^3 - R_1^3}{R_2^3}\right)$$

or

$$\left(\frac{R_1}{R_2}\right)_{cyl} = \left(1 - \frac{(\text{Void frac})_{cyl}}{0.908}\right)^{1/2}$$

$$\left(\frac{R_1}{R_2}\right)_{sph} = \left(1 - \frac{(\text{Void frac})_{sph}}{0.739}\right)^{1/3}$$

The calculation of efficiencies as a function of voltage and fuel layer thickness now follows immediately, utilizing the digital computer program described previously (RS 36-5). Ratios of the efficiencies for equivalent systems are then taken and, as indicated earlier, these efficiency ratios are approximately equal to the desired ratios of power per unit weight for equivalent systems on a constant power density assumption. Efficiency ratios vs void fraction are shown in Figures 4 and 5 for fuel layer thickness $\tau = 1$ fission fragment range and the range of voltages which appear possible in an actual reactor design. ($V = 1.0$ is the maximum voltage obtainable from fission
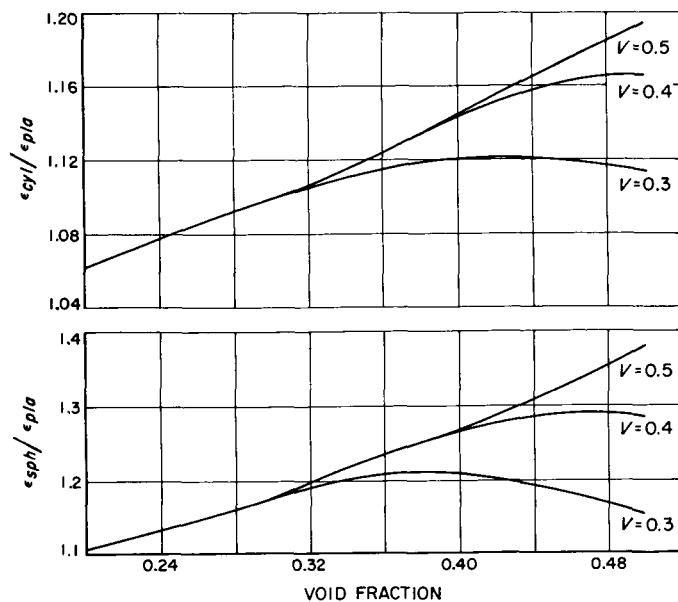
Figure 4. $\varepsilon_{cyl}/\varepsilon_{pl}$ vs void fraction for equal electrode separation and $\tau = 1.0$
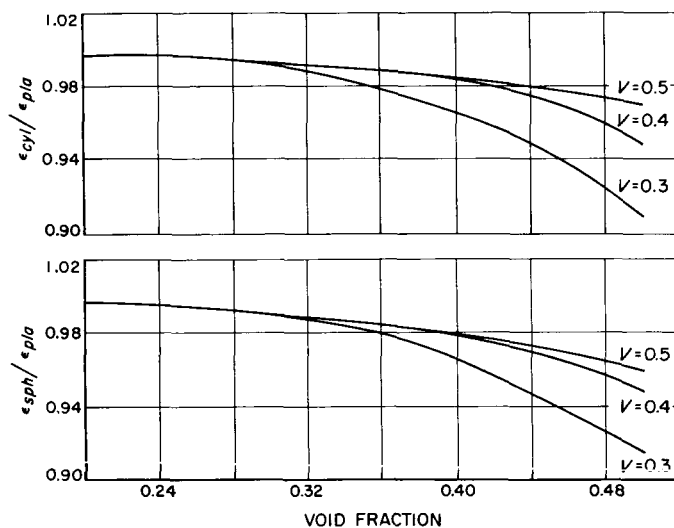
Figure 5. $\varepsilon_{cyl}/\varepsilon_{pl}$ vs void fraction for equal electric field and $\tau = 1.0$

fragments—approximately 4 mv.) Results for other layer thicknesses are quite similar.

b. Constant power per unit area of fuel surface. If the assumption is made that reactor power is limited by heat removal from the fuel layer, the ratio of the electric power per unit weight for two equivalent reactor systems of different geometry is no longer simply equal to their efficiency ratio, as it was under the constant power density assumption.

In accord with the assumptions listed earlier, the ratio of the electric power per unit weight in this situation can be written:

$$\frac{\left(\dfrac{\text{Electric power}}{\text{System weight}}\right)_1}{\left(\dfrac{\text{Electric power}}{\text{System weight}}\right)_2} = \frac{\varepsilon_1 P_1 \left[(Wt)_{reac} + (Wt)_{rad}\right]_2}{\varepsilon_2 P_2 \left[(Wt)_{reac} + (Wt)_{rad}\right]_1}$$

$$= \frac{\varepsilon_1 A_1 \left[(Wt)_{reac} + \alpha\left(\dfrac{P}{A}\right)A_2\right]}{\varepsilon_2 A_2 \left[(Wt)_{reac} + \alpha\left(\dfrac{P}{A}\right)A_1\right]}$$

where P/A is the power per unit area, here assumed constant.

It can be seen from the above expression that if the radiator weight is very much larger than the reactor weight, this ratio again reduces to $\varepsilon_1/\varepsilon_2$; the particular assumption made about reactor power limitation is not significant. However, where reactor weight is dominating, the ratio becomes

$$\frac{\varepsilon_1 A_1}{\varepsilon_2 A_2} = \frac{\varepsilon_1 \tau_2}{\varepsilon_2 \tau_1}$$

Actual cases will lie between these two extremes.

Without detailed knowledge of actual values for α and P/A, it is not possible to obtain power-to-weight ratios for the case of constant power per unit fuel area as was done above for the constant power density case. However, the two limiting cases of power-to-weight ratios,

$$\frac{\varepsilon_1}{\varepsilon_2} \quad \text{for} \quad (Wt)_{rad} >> (Wt)_{reac}$$

and

$$\frac{\varepsilon_1 \tau_2}{\varepsilon_2 \tau_1} \quad \text{for} \quad (Wt)_{reac} >> (Wt)_{rad}$$

are immediately available from the results of the constant power density case. The first limiting case is as already plotted in Figures 4 and 5; the second is shown in Figures 6 and 7.

It was found impractical and, in some instances, impossible to manage the entire problem analytically; so a program to obtain numerical solutions was prepared for the IBM 704 computer. This program determines R_1/R_2 and τ for equivalent reactors as shown above, then calculates their electrical efficiencies just as was done before (RS 36-5). The results shown in Figures 4 through 7 were obtained by means of this program.

Figure 6. $(\varepsilon_{cyl}/\varepsilon_{pl})$ (τ_{pl}/τ_{cyl}) vs void fraction for equal electrode separation and $\tau = 1.0$
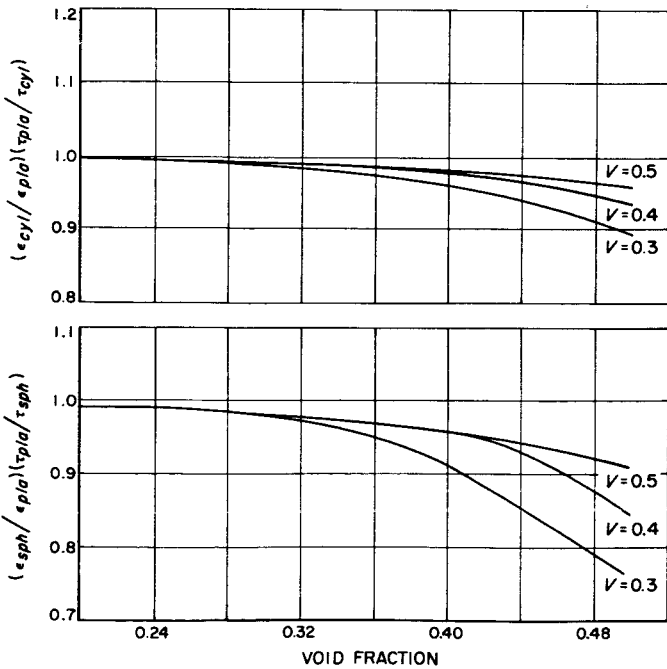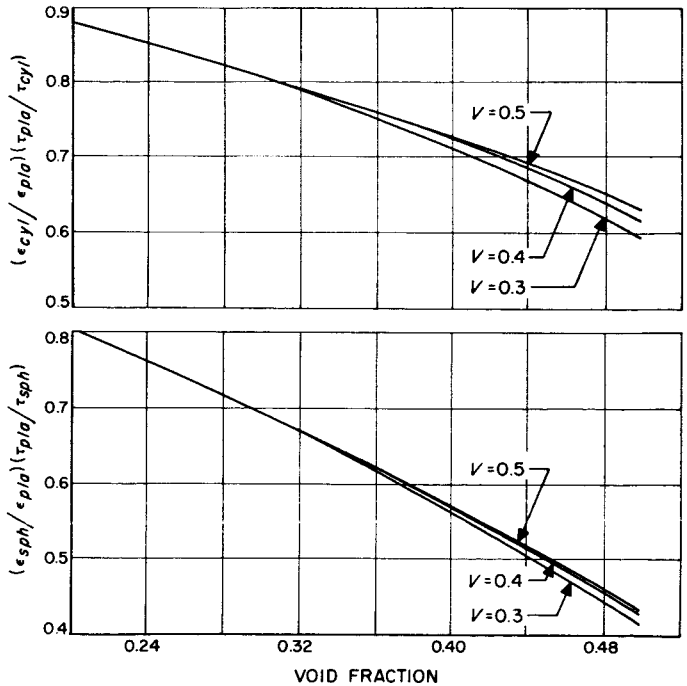

Figure 7. $(\varepsilon_{cyl}/\varepsilon_{pl})$ (τ_{pl}/τ_{cyl}) vs void fraction for equal electric field and $\tau = 1.0$

3. Conclusions

Considerable increases in the electrical efficiencies of fission electric cells occur in proceeding from plane electrodes, to cylindrical electrodes, to spherical electrodes, as observed previously (RS 36-5). The purpose of the present work was to ascertain how much effect this apparent improvement would have in an actual reactor system for space applications.

It is seen from the results displayed here that the increasing electrical efficiency due to geometric factors is unfortunately accompanied by a decreasing ratio of fuel surface to void volume which is due to these same geometric factors. Maintaining a constant fuel volume on the decreasing element area requires an increase in the fuel layer thickness which, of course, results in a reduction of electrical efficiency. Thus, the intended gains are largely lost and, as shown in Figures 4 through 7, the calculated power-to-weight ratios do not differ greatly for equivalent reactors of different cell geometry.

It seems clear, therefore, that the choice of fission cell geometry in a reactor for space application cannot be expected to greatly influence the actual power-to-weight ratio of the system; the choice of geometry can be made purely on a basis of engineering practicability.

II. Gas Dynamics Research

A. Liquid Sodium Flow Facility for Magneto-Fluid-Dynamic Research

Magneto-fluid dynamics is the field of study that results from the marriage of the two well-explored, but heretofore independent, disciplines of electrodynamics and fluid dynamics. It is concerned with the motion of conducting fluids (e.g., plasma, liquid metal, etc) in the presence of magnetic and electric fields. The coalition creates a many-fold increase in the complexity of the equations to be solved (a nonlinear coupling of the Navier-Stokes and Maxwell equations) and requires the adoption of stringent approximations in order to make even meager progress toward satisfactory theoretical solutions.

Experiments to check the validity of these approximate theories are virtually nonexistent and, with few exceptions, are of a qualitative, phenomenological nature. Experiments of an aerodynamic nature (e.g., flow about bodies in externally applied magnetic fields) have not been reported at all in the literature. To remedy the situation, a system has been designed to study, in a logical fashion, some of the implications of the interactions that result.

The wind tunnel is a familiar instrument in modern technology, and the present system is of the same generic type. A conducting fluid (liquid sodium at 150°C) is circulated in a closed loop, passing through the following components during its motion: a *free-surface* centrifugal pump, an electromagnetic flowmeter, a wide-angle diffuser and settling chamber, a nozzle, a test section, a narrow-angle diffuser, and a gas trap, finally returning to the pump suction. Reference to Figure 8 gives a complete picture of the arrangement of these components and of the fluid path. With pump speed control, throttling plus a bypass loop, the flow rate in the test section can be varied from 1 to 90 ft/sec. By a suitable arrangement of valves, the fluid can be filtered, and by manipulating pressures in the sump tank, expansion tank, and pump discharge, the system can be filled, pressurized to prevent cavitation in the test section, and emptied when maintenance is necessary. Emergency controls are incorporated so that the total sodium content can be dumped into the sump tank should leakage occur in any part of the system.

A magnetic field (produced by a current-carrying solenoid) fills the test section. The shape of the entry nozzle is designed to follow a chosen magnetic streamline, reducing *entry effects* that would otherwise be prohibitively large. Thus, the ideal conditions of current-free, vorticity-free flow in the test section are approached.

Instrumentation to be introduced into the test section is in the development stage; however, it is hoped that the following techniques can be used to gain a complete knowledge of the flow: (1) pitot-static tubes, (2) hot-wire and thin-film anemometers, (3) electromagnetic probes, (4) magnetometers, (5) pressure distribution measurements on body surfaces, (6) total lift and drag balances, and (7) flash X-ray photography of radio-opaque particles suspended in the fluid. A mechanism to traverse the probes longitudinally and radially has been designed.
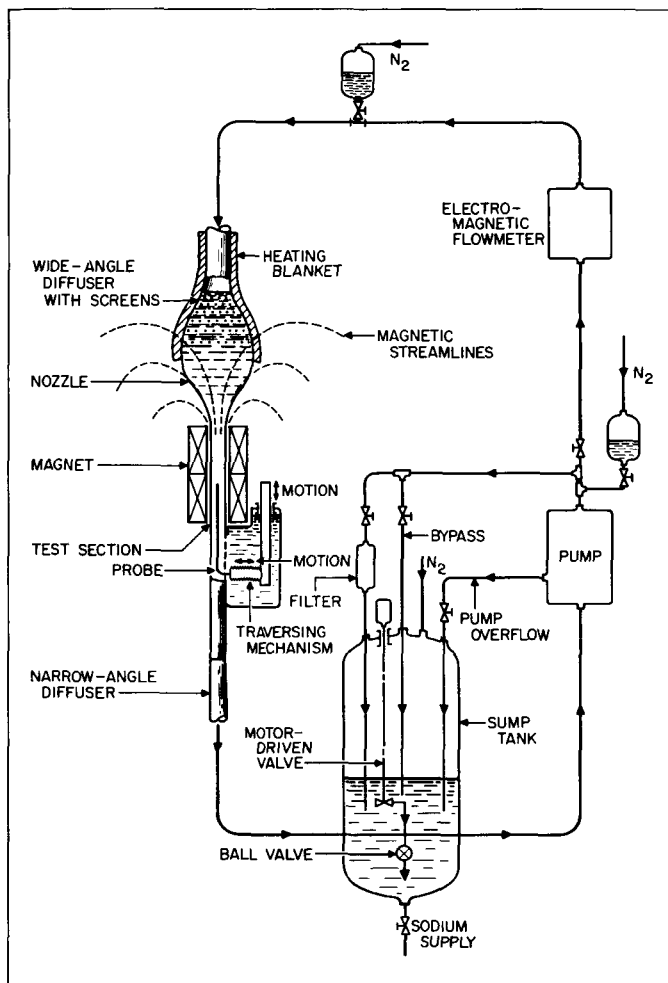
Figure 8. Liquid sodium flow facility

Many types of test are anticipated, at first with an aligned magnetic field (i.e., magnetic and flow streamlines parallel at test section entry) and later with crossed magnetic field (i.e., magnetic and flow streamlines perpendicular at entry). These include (1) flow about various solid body shapes, especially to verify the existence of the predicted precursive disturbance, and to find the dependence of drag, separation and vortex formation on the magnetic field; (2) structure and stability of boundary layer flow; and (3) characteristics of magneto-turbulence.

The effects of magnetic fields of local origin (e.g., the field produced by a current-carrying elliptic cylinder) and the effects of local fields that introduce no solid bodies into the flow (e.g., the field produced across the pole pieces of a small electromagnet) are of interest.

It is anticipated that extensive applications will be found for the system.

B. Piezo-Electric Probe for Measurement of Static Pressure Fluctuations in Turbulent Air Flow

Since a knowledge of the variation of the statistical properties of static pressure fluctuations throughout a turbulent flow field and their correlation with velocity fluctuations could lead to a materially improved understanding of the mechanisms of turbulence, an attempt has been made to construct a probe which could be used for such measurements. Ideally, it would be desirable to have a device which would respond only to fluctuations in static pressure, but in practice, due to flow perturbations associated with the probe and the sensitivity of piezo-electric crystals to accelerations as well as pressures, this ideal can not be realized. The methods used to deal with these problems are discussed in this Summary.

1. Probe Vibration Effects

Since the electrical output of a piezo-electric crystal depends on the stress applied to it, the crystal cannot distinguish between stresses of hydrodynamic origin and inertia stresses resulting from vibration of the crystal mounting. An early design of probe consisted of a single crystal set with a peripheral rubber support in a small metal cantilever. When this probe was placed in a turbulent air jet, its signal output was dominated by a set of discrete frequency components corresponding to the natural frequencies of the supporting cantilever. Attempts to design a probe with its lowest natural frequency sufficiently high to be above the frequency range of interest in most turbulence applications (greater than, say, 50 kc) were unsuccessful.

These considerations led to the adoption of a probe with a pair of crystals mounted with faces of like polarity attached to the support (Fig 9). With this arrangement, vibration of the probe in a plane parallel to the direction of polarization of the crystals gives rise to a tensile inertia stress in one crystal and a compressive stress in the other, and vice versa, so that the vibration signals from the two crystals are 180 degrees out of phase. Thus, by addition of the two crystal outputs, the vibration signals can be cancelled. The resulting signal then represents the sum of the hydrodynamic pressures on the two exposed crystal faces, provided that the sensitivity of the crystals to stresses in the transverse direction is sufficiently small to make (in-phase) signals from this source small compared to the pressure signals of interest, a condition which appears to be satisfied in practice.
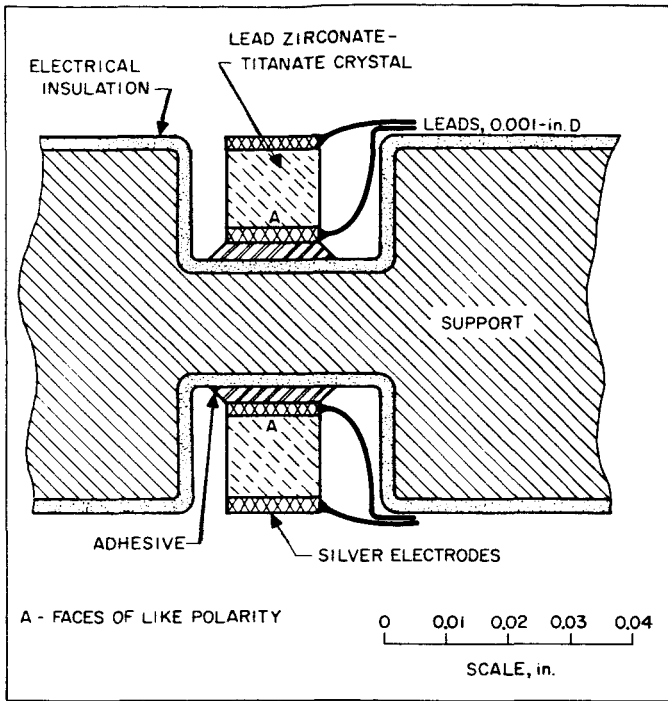
Figure 9. Transducer construction detail

Preliminary experiments with a two-crystal probe excited by jet turbulence showed that, with the use of a differential-gain adding circuit, vibration signals could be successfully eliminated.

2. Probe Output

To consider the effect on crystal output of flow perturbations (predominantly of the cross-flow v and w velocity components) due to a slender probe, the following assumptions are made:

(1) The crystals are located sufficiently close to the nose of the probe that no separation of the cross-flow occurs, in which case the probe may be considered subject to a potential cross-flow.

(2) The physical dimensions of the probe are sufficiently small to allow the flow field around it at any instant to be considered uniform.

(3) The cross-flow is incompressible.

Let v, w be the fluctuating components of velocity transverse to the mean-flow, and let

$$V^2 = \tfrac{1}{2}\rho\,(v^2 - \langle v^2 \rangle); W^2 = \tfrac{1}{2}\rho\,(w^2 - \langle w^2 \rangle);$$
$$X = \tfrac{1}{2}\rho\,(vw - \langle vw \rangle)$$

P = static pressure = $\langle P \rangle + p$

p = static pressure fluctuation

ρ = fluid density

s = crystal sensitivity, voltage/unit pressure

$\langle\ \rangle$ = denote a statistical mean value

Consider first the output of a single crystal, with probe orientation as shown in Figure 10. Using the well-known result for the potential-flow pressure distribution around a circular cylinder, the instantaneous pressure on the crystal is given by

$$P' = P + \tfrac{1}{2}\rho\,(v^2 + w^2)\,[1 - 4\sin^2(\alpha + \gamma)]$$
$$= P - \tfrac{1}{2}\rho\,(v^2 + w^2)$$
$$+ \rho\,(v^2 + w^2)\,(\cos 2\alpha \cos 2\gamma - \sin 2\alpha \sin 2\gamma)$$
$$= P - \tfrac{1}{2}\rho\,(v^2 + w^2) + \rho\,[(w^2 - v^2)\cos 2\gamma - 2vw \sin 2\gamma]$$

since $\tan \alpha = v/w$; $\sin 2\alpha = 2vw/(v^2 + w^2)$; $\cos 2\alpha = (w^2 - v^2)/(v^2 + w^2)$, with the mean value

$$\langle P' \rangle = \langle P \rangle - \tfrac{1}{2}\rho\,(\langle v^2 \rangle + \langle w^2 \rangle)$$
$$+ \rho\,[(\langle w^2 \rangle - \langle v^2 \rangle)\cos 2\gamma - 2\langle vw \rangle \sin 2\gamma]$$

If the inertia stresses in the crystal due to probe vibration are equivalent to an additional fluctuating pressure Y, ($\langle Y \rangle = 0$), then, since the crystal responds only to fluctuations, its instantaneous voltage output is

$$e_1 = s_1\,(P' - \langle P' \rangle + Y)$$
$$= s_1\,\{p - (V^2 + W^2)$$
$$+ 2\,[(W^2 - V^2)\cos 2\gamma - 2X \sin 2\gamma] + Y\} \quad (1)$$

Similarly, the output of a crystal at angle $(\gamma + \pi)$ is

$$e_2 = s_2\,\{p - (V^2 + W^2)$$
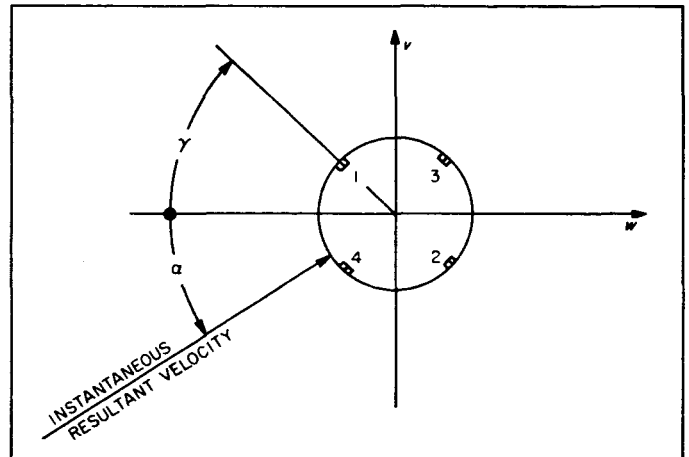$$+ 2\,[(W^2 - V^2)\cos 2\gamma - 2X \sin 2\gamma] - Y\} \quad (2)$$

Figure 10. Cross-flow geometry

From Equations (1) and (2)

$$e_{1,2} = s_2 e_1 + s_1 e_2 = 2 s_1 s_2 \{ p - (V^2 + W^2)$$
$$+ 2[(W^2 - V^2) \cos 2\gamma - 2X \sin 2\gamma] \} \quad (3)$$

as the voltage output of the crystal pair with vibration cancellation.

The corresponding output for a pair of crystals located at $(\gamma + \pi/2)$ and $(\gamma + 3\pi/2)$ is

$$e_{3,4} = 2 s_3 s_4 \{ p - (V^2 + W^2)$$
$$- 2[(W^2 - V^2) \cos 2\gamma - 2X \sin 2\gamma] \} \quad (4)$$

By combining the outputs of the two crystal pairs, the instantaneous signal

$$(s_3 s_4 e_{1,2} + s_1 s_2 e_{3,4} = 4 s_1 s_2 s_3 s_4 [p - (V^2 + W^2)] \quad (5)$$

is obtained which is independent of the rotation of the probe about its longitudinal axis. This has obvious advantages insofar as angular alignment of the probe is concerned, but in practice it may be more convenient to waive this advantage and use some other combination of $e_{1,2}$ and $e_{3,4}$. For example, if $\gamma = 0$, then

$$e_{1,2} = 2 s_1 s_2 (p - 3V^2 + W^2) \quad (6)$$

$$e_{3,4} = 2 s_3 s_4 (p + V^2 - 3W^2) \quad (7)$$

and the following combinations are obtainable:

$$(3 s_3 s_4 e_{1,2} + s_1 s_2 e_{3,4}) = 8 s_1 s_2 s_3 s_4 (p - 2V^2) \quad (8)$$

$$(s_3 s_4 e_{1,2} + 3 s_1 s_2 e_{3,4}) = 8 s_1 s_2 s_3 s_4 (p - 2W^2) \quad (9)$$

Using two crystal pairs only, it is not possible to generate the instantaneous value of p; in principle, this could be done by using three crystal pairs, but the procedure implies a long chain of electronic circuits and presupposes a prior knowledge of the mean values $\langle v^2 \rangle$, $\langle w^2 \rangle$, and $\langle vw \rangle$. Any further increase in the number of crystal pairs is not fruitful, since any combination of signals which eliminates vw terms leads back essentially to the relations expressed by Equations (5), (8), (9), while combinations which do not eliminate these terms lead to electronic complications as in the case of three crystal pairs. Thus, there is little point in increasing the number of crystals beyond four, in which case, to obtain mean-square pressures or pressure-velocity correlations it becomes necessary to use the probe in conjunction with hot wires.

Suppose $\langle p^2 \rangle$ is required, then, taking for example Equation (8)

$$\frac{\langle (3 s_3 s_4 e_{1,2} + s_1 s_2 e_{3,4})^2 \rangle}{8 s_1 s_2 s_3 s_4} = \langle p^2 \rangle - 4 \langle pV^2 \rangle + 4 \langle V^4 \rangle \quad (10)$$

For the case of a turbulent boundary layer, the three terms on the right-hand side of Equation (10) can be of the same order and, hence, to obtain $\langle p^2 \rangle$ the other two must be known. Now

$$\langle p^2 \rangle - 4 \langle pV^2 \rangle + 4 \langle V^4 \rangle = \langle p^2 \rangle - 4 \langle (p - 2V^2) V^2 \rangle - 4 \langle V^4 \rangle$$

and $\langle (p - 2V^2) V^2 \rangle$ can be obtained from correlation of probe of hot wire signals and $\langle V^4 \rangle$ from hot wire measurements only. (The possibility remains, of course, that $\langle pV^2 \rangle$, which at present is an unknown correlation, is small compared to the other two terms, in which case $\langle p^2 \rangle$ could be obtained from independent measurements with the probe and hot wires.)

3. Status of Experiments

The probe in its present form is shown in Figure 11. It has four square lead zirconate-titanate crystals $0.015 \times 0.015 \times 0.018$ inch thick mounted symmetrically in a cylindrical probe 0.060 inch in diameter. The details of the mounting are as shown in Figure 10. A schematic representation of the instrumentation is shown in Figure 12. The correct relative gain settings of the amplifiers before the first adding units are obtained by adjusting to give vibration cancellation (which can be determined satisfactorily by observation of the signal spectrum on a Panoramic analyzer). To obtain the required gain settings before the final adding unit, it is necessary to take advantage of any existing symmetries of the flow under investigation or equalize signals from the probe in its normal position and rotated through 90 degrees about its longitudinal axis.

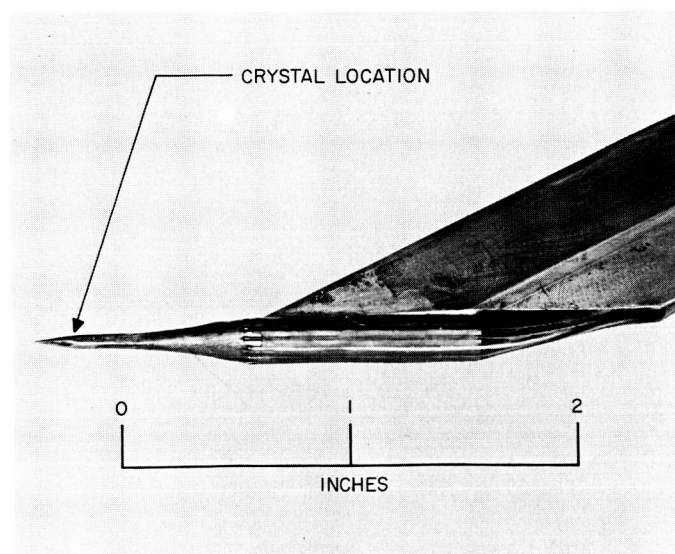The probe and associated apparatus are now being tested in jet turbulence.

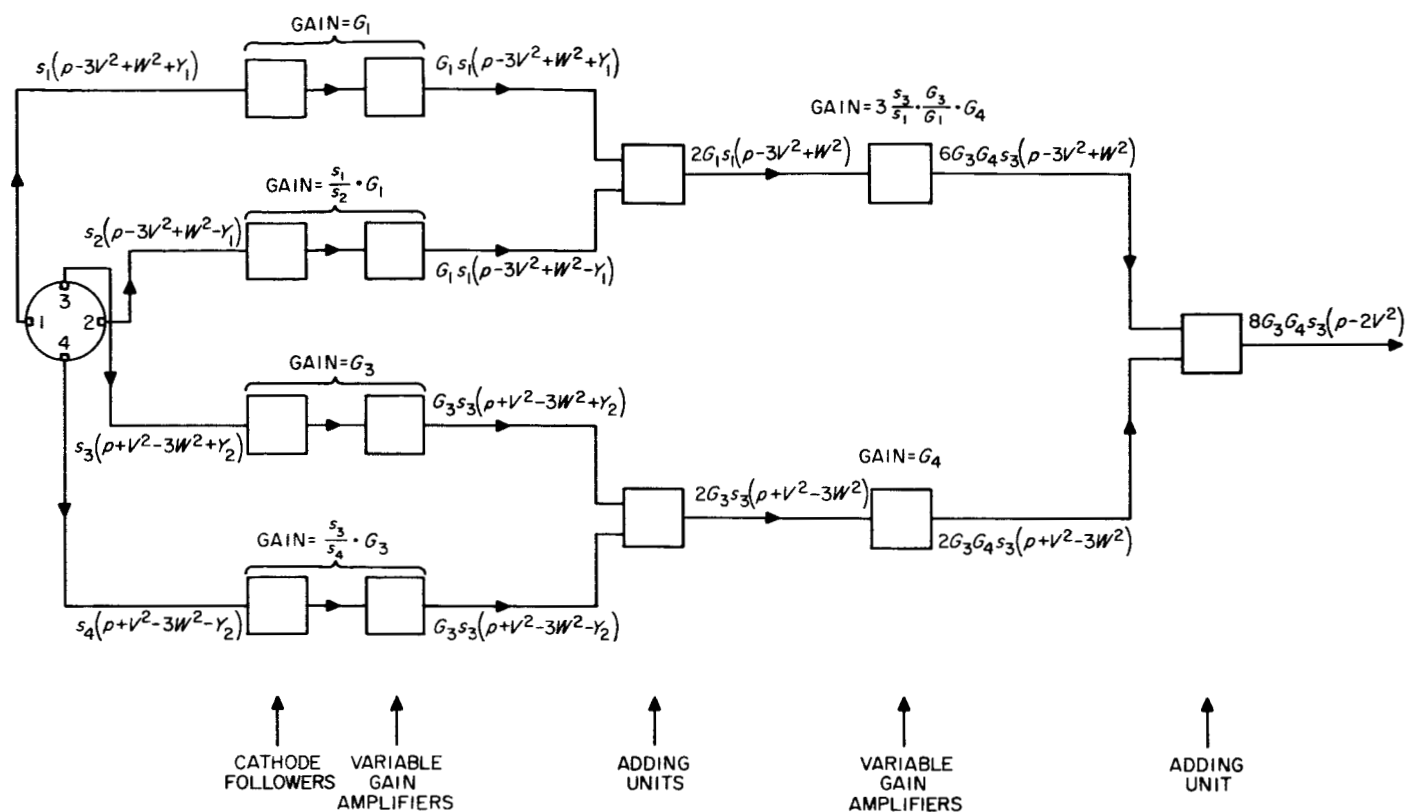Figure 11. Static pressure probe

Figure 12. Block diagram of circuitry to obtain $(p - 2V^2)$

ENGINEERING MECHANICS DIVISION

III. Materials Research

A. Graphite

1. Graphite Tension Testing

Determination of elevated temperature tensile properties of pyrolytic graphite has been continued on several blocks of material produced by the General Electric Company and supplied by Lockheed Missile and Space Division Re-entry Systems. These tensile tests, according to the supplier, were for the purpose of noting lot-to-lot variations. The room temperature tests were made using an Instron testing machine. Elevated temperature tests were made using testing equipment previously described (RS 36-3).

Tensile data for these tests are presented in Table 2. The room temperature strength data for Lot 158 is seen to show greater scatter than for Lot 160. The average strengths for these lots are 15,700 and 15,800 psi, respectively. Two of the three Lot 159 room temperature tests (2950, 2951) are thought to be invalid. One specimen fractured outside the gage section and the other specimen fractured in several places along the gage section. Presumably, both specimens were cracked prior to testing.

Of the 3000°F tests, Lot 160 shows the least scatter but has a lower average ultimate tensile strength than Lots 158 and 159. Evaluation of the 5000°F tests is difficult because the pull rods, rather than the tensile specimens, broke.

Instron cross-head movements were used as a measurement of elongation in the room temperature tests. The recorded elongation presented in Table 2 includes the strain due to specimen load train tightening and specimen seating as well as specimen strain. Further investigation into the magnitude of strain due to the former two factors is needed in order to evaluate and compare room temperature strain data.

The recorded elongations for the 3000°F and higher temperature tensile tests are complicated by several factors. The precision in strain measurement is ±2%. This means that the recorded elongations for the 3000 and 4000°F tests may be in error by this order of magnitude. The upper limit in the strain measuring equipment is 60%. Above this value the recorded elongations may be in error by greater than 2%. It is suspected, however, that the recorded elongations for the 5000°F tests are slightly higher than the actual values. The present strain measuring equipment is being re-examined for possible ways of increasing the precision and extending the range.

It has been previously reported (CBS 56) that the bulk density of pitch-coke graphites decreases during tensile deformation. Preliminary bulk density measurements on pyrolytic graphite, as shown in Table 3, also indicate that the bulk density of this material decreases with tensile deformation. This decrease in bulk density is very slight, if any, after deformation at room temperature and 3000°F but is most pronounced after deformation at

5000°F. Layer plane delaminations of pyrolytic graphite are apparently responsible for the bulk density change.

Also presented in Table 3 is the change in apparent density with deformation as measured in CCl_4. No appre-

Table 2. Pyrolytic graphite tension test data

Lot[a] No.	Specimen No.	Test temperature, °F	Ultimate tensile strength, psi	Recorded elongation, %
158	2939	RT	19,000	3.0
	2940	RT	15,200	1.8
	2941	RT	13,100	1.6
159	2950	RT	6,200	1.4
	2951	RT	7,000	1.8
	2952	RT	12,100	2.6
160	2962	RT	16,600	2.6
	2963	RT	16,900	2.4
	2964	RT	14,000	2.9
158	2942	3000	18,800	2.3
	2943	3000	21,500	3.0
	2947	3000	23,400	3.2
159	2953	3000	22,000	3.4
	2954	3000	17,800	2.7
	2961	3000	16,000	1.3
160	2965	3000	15,500	2.3
	2966	3000	16,200	3.4
	2969	3000	14,600	2.4
159	2956	4000	23,400	4.2
	2959	3590	16,800	2.2
	2960	4000	22,000	2.1
158	2944	5000	71,000	70
	2945	5000	>62,000[b]	>61[b]
	2946	5000	>73,200[b]	>46[b]
159	2957	5000	>65,000[b]	>68[b]
	2958	5000	64,000	113
160	2967	5000	>90,000[b]	>139[b]
	2968	5000	71,000	81
	2970	5000	78,000	57

[a]Material produced by General Electric Company and supplied by Lockheed Missile and Space Division Re-entry Systems.
[b]Pull rod broke during test; strength and elongation greater than values reported.

Table 3. Pyrolytic graphite bulk and apparent densities before and after deformation

Lot No.	As deposited	Test temperature		
		RT	3000°F	5000°F
Bulk density, gm/cm³				
158	2.198	2.12	2.15	1.98
159	2.183	2.18	2.15	2.10
160	2.189	2.15	—	2.04
Apparent CCl_4 density, gm/cm³				
158	2.205	2.207	2.198	2.252
159	2.197	2.204	2.209	2.254
160	2.204	2.203	—	2.247

ciable change is observed after deformation at room temperature and 3000°F; however, after deformation at 5000°F marked increases are observed and these density values are seen to approach the theoretical density for graphite. The increase in apparent density is due to marked structural changes, previously reported (RS 36-3, 36-4, 36-5), which accompany deformation at 5000°F.

The structural changes reported earlier (RS 36-3, 36-4, 36-5) suggested that pyrolytic graphite that has been deformed at 5000°F, but has not fractured, should become stronger when tested at lower temperatures than non-deformed material. Several tests were made in which the pyrolytic graphite was prestrained at 5000°F and then tested at 4000°F. These data, along with tests made at 4000°F without prior prestraining at 5000°F, are given in Table 4. It is seen that Block 14601 is at least twice as strong at 4000°F after prestraining. Block 14701, on the other hand, becomes 3.5 to 4 times stronger at 4000°F after prestraining. Prestraining Block 14701 to 41% is seen to result in a stronger pyrolytic graphite than 13% prestraining. This unusual behavior of pyrolytic graphite which is similar to metals suggests that the strength of this material may be increased by hot-working.

Table 4. Pyrolytic graphite tensile data after prestraining

Block No.	Prestrain test				4000°F test	
	5000°F		4000°F		Ultimate tensile strength, psi	Measured elongation, %
	Maximum stress, psi	Measured elongation %	Ultimate tensile strength, psi			
14601	29,500	~35	>47,000[a]		24,400	—
14701	37,000	13	49,100		12,600	0.3
14701	59,000	41	56,100		13,600	0.7

[a]Pull rod broke.

B. Endothermal Materials

1. Tungsten Lamp Furnace

An experimental transient heating method to determine constant values of thermal conductivity over a range of elevated temperatures has been applied to three commercial plastics for the purpose of determining the suitability of the experimental method in obtaining usable, reliable data. A tungsten-lamp furnace, previously

described in *RS 36-4*, and a specimen holder assembly shown schematically in Figure 13 were used. The experimental assembly consisted of two 3- × 3- × 0.125-inch plastic specimens surrounding a copper block 3- × 3- × 0.25-inch, secured in the holder by the support of two 4- × 4- × 0.125-inch aluminum outer plates. Thermocouples were positioned on the plastic specimen surfaces at their geometrical centers beneath the outer aluminum support plates to measure and control the hot wall temperature; a third thermocouple, to measure the cold wall temperature, was within the geometrical center of the copper block. These thermocouples were monitored continuously with a recording oscillograph. Glass wool
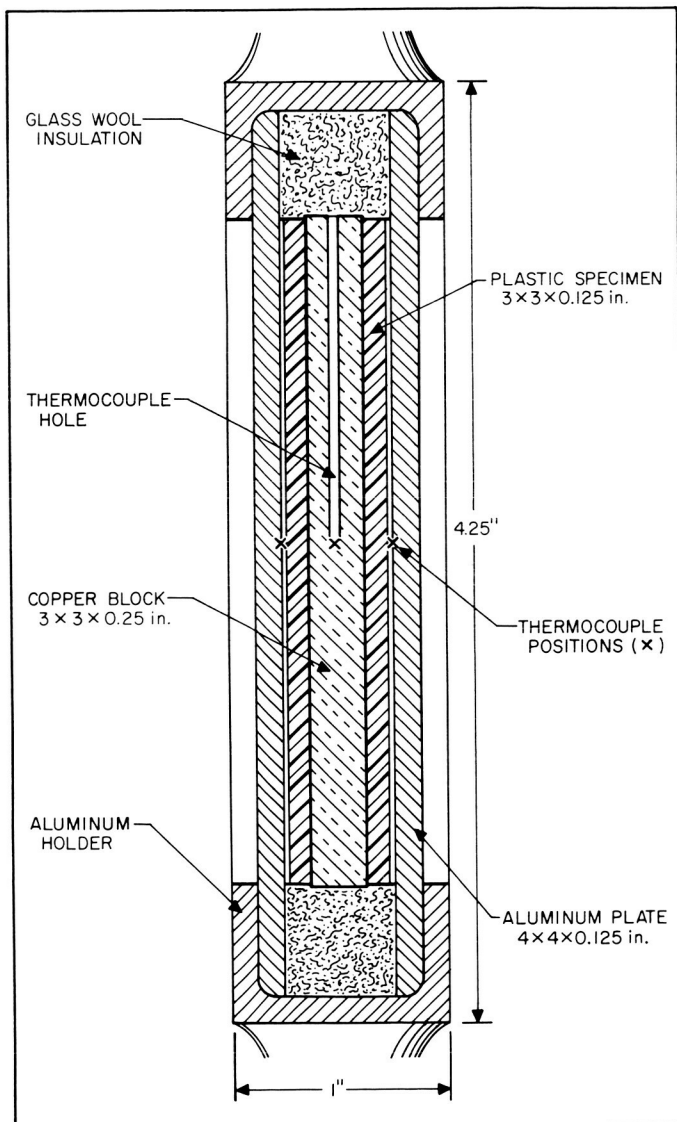
insulation along the sides of the holder helped prevent extraneous heat flow to the copper block. A view of the holder partly disassembled is shown in Figure 14.

In a typical experiment, the hot-wall temperature was raised to and held constant at a predetermined value somewhat less than the minimum temperature at which thermal degradation of the plastic material involved could occur, thus establishing equal thermal gradients between the hot wall and the cold wall. When the temperature differential between the hot wall surfaces and the cold wall of the copper block had decreased to about 15°F, usually in 10 minutes, the test was ended.

The thermal conductivity and thermal diffusivity were then calculated. In these calculations, the copper block and specimen dimensions, literature values of their densities and specific heats, and the experimental temperature–time data were used according to the method outlined in Reference 5. In the application of this experimental method the results of these tests produced a single value of the thermal conductivity of the material which is constant over a limited range of temperatures. The temperature range is defined as the cold-wall temperatures over which the logarithm of the ratio $(T_0 - t)/(T_0 - t_0)$ plots as a straight line against time, where T_0 is the constant hot wall temperature, t_0 is the initial uniform temperature of the specimens and copper block, and t is the temperature of the cold wall at any time after the start of the experiment. If the function is not a straight line with time, the thermal conductivity is not constant.
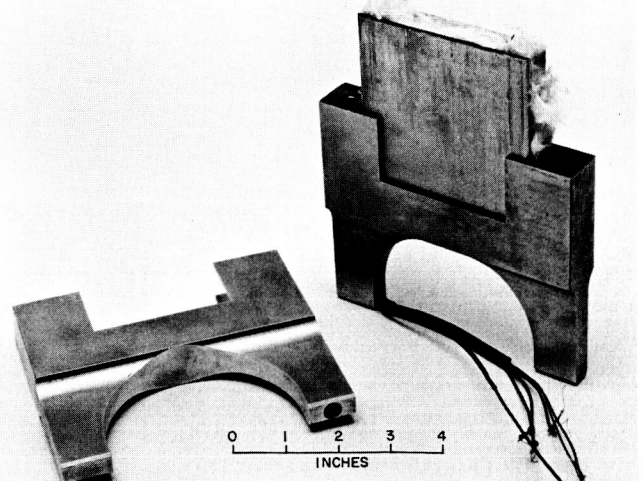

Figure 13. Cross-sectional drawing of specimen holder assembly for radiant heating furnace

Figure 14. View of specimen holder assembly for radiant heating furnace

The experimental thermal conductivity and thermal diffusivity of commercial polyethylene, polytetrafluoroethylene, and polymethylmethacrylate are shown in Table 5. Also shown in Table 5 are the room temperature thermal conductivity and thermal diffusivity of comparable plastics as given in the literature (Ref 6). The somewhat lower values of the experimental results, when compared with the room temperature literature values, may indicate a decrease in the thermal properties with increase in temperature. Experiments with plastics at values of T_0 lower than in the experiments reported herein will be made to determine thermal conductivity in intermediate temperature ranges between the maximum temperatures at which the plastics are thermally stable and room temperature. A decrease in thermal conductivity and, thermal diffusivity with increasing temperature in certain reinforced thermosetting plastics is given by Mixer and Marynowski (Ref 7).

2. Plasma Generator

Calibration continues on the 600-kw plasma generator facility described earlier (RS 36-4), using argon as a working fluid and a thoriated tungsten cathode in conjunction with a 0.5-inch throat, sonic exit nozzle. Preliminary DC power input curves for the tungsten-argon system, similar to those for carbon-nitrogen (RS 36-6), are shown in Figure 15. These curves represent the actual power imparted to the generator, before cooling losses, for a specific setting of the power supply transformer coils and for changing working fluid flow rates. Figure 16 shows the voltage-current characteristics for the same operating conditions.

Figure 15. Input power characteristics for plasma generator with tungsten—argon system

Table 5. Experimental values at elevated temperature of thermal conductivity and thermal diffusivity of certain commercial plastics compared to literature values at room temperature

Commercial plastic	Thermal conductivity, Btu/hr-ft²-°F/ft	Thermal diffusivity,[c] ft²/hr	Cold-wall temperature, °F
Polyethylene, medium density	0.19[a] 0.17[b]	0.0059 0.0053	Room 150–170
Polytetrafluoro-ethylene	0.15[a] 0.14[b]	0.0045 0.0041	Room 277–353
Polymethyl-methacrylate	0.10–0.15[b] 0.11[b]	0.0039–0.0058 0.0043	Room 138–164

[a]Reference 6.
[b]Experimental values.
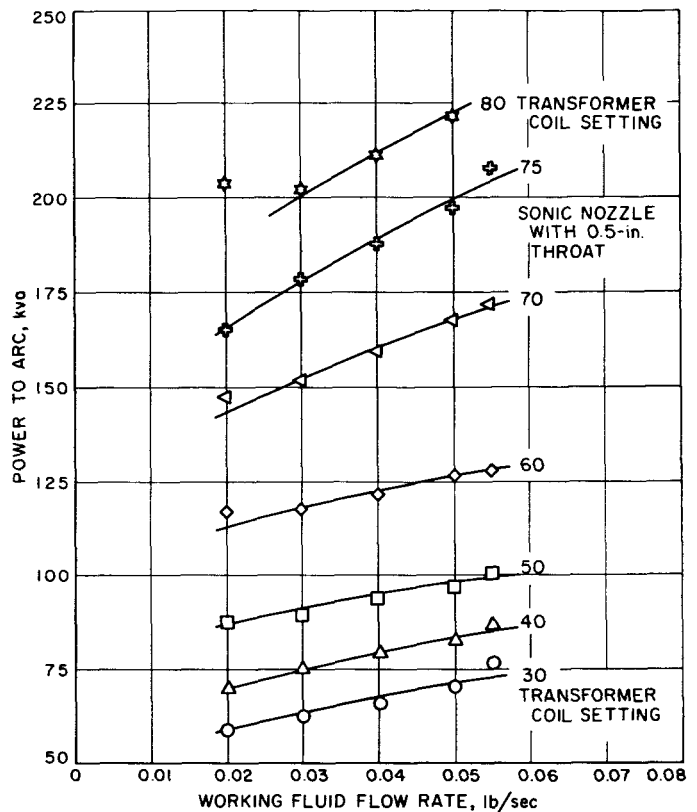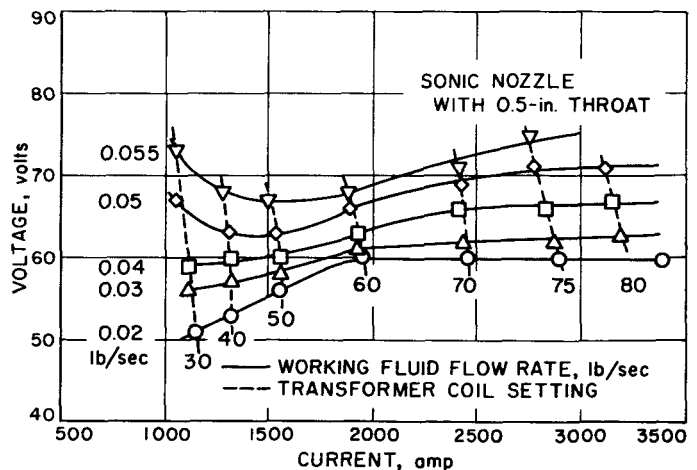[c]Calculated from thermal conductivity values.

Figure 16. Current-voltage characteristics for plasma generator with tungsten—argon system

IV. Applied Mathematics

A. Numerical Analysis

1. Variable End Point Method for Solution of Boundary Value Problems

A common technique for solving two-point boundary value problems for systems of ordinary differential equations is to solve the associated initial value problem for assumed values of the initial conditions, correcting the assumed initial values by differential correction techniques until the desired end-point conditions are met. The method may fail to converge because of extreme nonlinearity between the desired conditions and the assumed initial values. In particular, for systems with more than two or three degrees of freedom, it is often necessary to start the iteration rather close to the actual solution in order to get convergence, although the rate of convergence, once a reasonably good approximation has been found, is quite fast.

A modification of this procedure which, in essence, directs the search for good starting values has been developed in connection with solving a particular problem arising in plasma physics. It may be described in a general setting as follows:

Suppose that a system of first-order differential equations is given

$$\frac{dx}{dt}i = f_i(x_1, \cdots, x_n; t) \, i = 1, \cdots, n \qquad (1)$$

subject to n independent linear boundary conditions:

$$\sum_{j=1}^{n} [a_{ij} x_j(t_0) + b_{ij} x_j(T)] = c_j i = 1, \cdots, n \qquad (2)$$

where the solution is desired, of course, for $t_0 \leq t \leq T$. In most applications, $m < n$ of the restraints will be of the form

$$x_i(t_0) = c_i, i = 1, \cdots, m$$

The difficulty of solution by numerical techniques depends in part on the integration range. Thus, consider T as a parameter of the problem; then if the length of the interval $t_1 - t_0$ is small, the solution of Equation (1) subject to the boundary conditions (2) with $T = t_1$ is found by the usual process of differential corrections. This solution yields good first approximations to the initial conditions for the solution of (1) subject to (2) with $T = t_2 > t_1 > t_0$. Iteration of this technique may then permit extension to the desired range (t_0, T).

It is seen that the search among $n - m$ parameters for the *right* initial conditions is in this way narrowed to a succession of searches contained in a relatively narrow tube in E_{n-m}. The technique is evidently akin to analytic continuation.

It has been found in application that a single application of the differential correction scheme is enough to advance the solution from the interval (t_0, t_j) to the interval (t_0, t_{j+1}) for quite reasonable separation of the points t_j and t_{j+1}. Moreover, extrapolation along the directions

determined by the initial conditions necessary to solve (1) subject to (2) for $T = t_j, t_{j-1}, \cdots$ permits even better first guesses at the initial conditions necessary to solve (1) with $T = t_{j+1}$. However, the method fails if the solution on (t_0, t_k) fails to exist for some t_k which has happened in isolated cases. The difficulty can usually be overcome by choosing a new first point closer to the desired end point.

B. Computer Operations

On November 21, 1960 the IBM 7090 computer system arrived at JPL, and installation began. The 7090 was installed in the same location as that occupied by the 704 which was returned to IBM. However, the computer work load was such that it was highly desirable to keep the 704 operating during the installation period for the 7090. Although the equipment configurations were completely different, by regrouping the 704 it was possible to keep the 704 operating in an overcrowded situation for all but 2 days of the installation period. The 704 was dismantled and returned to IBM on December 7, 1960; the 7090 was accepted by JPL for lease on December 9, 1960. For the next 3 weeks, there were many component failures in the computer system, and over-all system availability was low. However, toward the end of December 1960, the failures were decreasing and the computer system was becoming a reliable system.

The transfer of programs to the IBM 7090 actually began in September 1960, and the 709 computer at UCLA and the 7090 at Rocketdyne were used to check out the programming systems and some production programs. However, the bulk of the programs was not converted to 7090 systems and checked out when the machine arrived. Productive computing was possible for all programs that had been checked out and operating on the 704 by using a compatibility program which allows the 7090 to execute 704 programs directly. By the end of December, most of the programs were in checkout in 7090 programming systems, and full conversion to the 7090 was expected to be complete by the end of January.

At the same time the 7090 was installed, an off-line card to magnetic tape system was delivered. This equipment was necessary to eliminate the reading of punched cards by the 7090, which is an extremely slow operation compared with the computing speeds of the 7090.

The IBM 704 had been at JPL for 2 years at the time of its replacement by the 7090. The computing load on the 704 had grown to a 24-hour/day, 5-day/week operation. Table 6 summarizes the 704 computing load for the period January 1, 1960 through December 1, 1960. Of the total scheduled time, the 704 was available 89% of the time. Of the total available time, 61% was spent in productive computing and 39% was in translation from programming language to machine language and checkout of the resulting programs. Miscellaneous time represents idle time; i.e., bad time due to card jams, magnetic tape breakage, and time spent in checking out programming systems.

The ElectroData computer completed its sixth full year of operation. Table 7 summarizes the operation of the EDC computer for the year of 1960. The primary use of the EDC was for wind tunnel data reduction and solid

Table 6. IBM 704 time distribution for period January 1, 1960 to December 1, 1960

Month	Assembly, hr	Fortran, hr	Code check, hr	Production, hr	Scheduled maintenance	Unscheduled maintenance	Misc, hr	Total, hr
Jan	25	5	84	185	23	31	40	393
Feb	27	3	75	178	22	25	36	366
Mar	43	6	101	167	24	54	22	417
Apr	39	4	95	297	20	14	34	503
May	38	11	90	302	15	23	37	516
June	43	15	99	257	19	27	23	483
July	33	15	106	189	13	55	34	445
Aug	30	25	124	210	21	27	59	496
Sept	29	20	121	224	17	38	26	475
Oct	27	24	119	310	16	41	29	566
Nov	23	25	179	260	7	40	29	563
Total	357	153	1193	2579	197	375	369	5223

Table 7. EDC time distribution for period January 1, 1960 to December 31, 1960

Month	Code check, hr	Production, hr	Maintenance, hr	Total, hr
Jan	34.6	138.8	15.1	188.5
Feb	35.3	60.5	18.3	114.1
Mar	52.5	92.1	44.1	188.7
Apr	48.6	121.9	20.7	191.2
May	40.2	124.8	21.2	186.2
June	24.4	151.1	23.3	198.8
July	53.0	100.5	15.0	168.5
Aug	37.4	139.2	30.6	207.2
Sept	17.5	132.7	38.5	183.7
Oct	39.5	136.9	18.2	194.6
Nov	24.7	110.0	19.5	154.2
Dec	14.5	124.0	23.8	162.3
Total	422.2	1432.5	288.3	2143.0

Table 8. Summary of analog computer operations for 1960

Quarter	Analysis and programming, man-days	Computer time, console-days	Total, days
1st	20.1	35.5	55.6
2nd	18.1	31.6	49.7
3rd	63.5	66.3	129.8
4th	48.5	95.9	144.4
Totals	150.2	229.3	379.5

propellant data reduction. The performance continued to be reliable with an availability of 87%. It should be noted that no time is recorded for translation from a programming language to machine language since the programs are written directly in machine language.

The Analog Computing Center of JPL has completed over 10 years of operations and its sixth year at its current location. The present facility consists of four consoles of Electronic Associates computing equipment incorporating 250 operational amplifiers with a complete complement of nonlinear components.

Table 8 is a summary of operations for 1960. Due to abrupt changes in Laboratory programs and organization during 1959 and early 1960, the analog computer work load was light. During the second half of the year, the need for analog computing increased.

C. Data Handling Systems

The efficient utilization of general purpose computers in reducing experimental data depends upon the availability of a recording system for the recording of experimental measurements on a medium that the computer is capable of directly utilizing. With high-speed computers, magnetic tape is the most desirable input medium since input speeds are more compatible with internal computational speeds.

Magnetic tape is often the most desirable form of recording media for recording of test results due to its speed and its capability of recording large volumes of data. However, the available digital recording systems are usually designed for a specific recording problem and are not mobile for miscellaneous test data recording.

A general purpose data system has been designed and is now available. This system is a mobile digital data system with the capability of sampling one channel of analog data and recording this data on magnetic tape in a digital format compatible with the IBM 7090 computer. A multiplexer is currently being added which will allow the sampling of up to 10 analog channels and recording on magnetic tape. In addition to the recording of analog information, the system will read paper tape and translate the information onto magnetic tape. It will also read magnetic tape and punch paper tape, making the IBM 7090 available for reduction of data recorded on paper tape. Figure 17 is a photo of the general purpose digital data logger (Digilog Data System).

Figure 18 is a block diagram of the Digilog system. The analog-to-digital converter is an Epsco Transicon Datrac TD703S with an accuracy of 0.05% for a ± 10-volt full-scale input. Conversion rate is variable from 0 to 3000 samples/sec. A sample consists of three decimal digits plus sign. Digital data from the converter is stored in a magnetic core buffer memory with a capacity of 1026 characters or 171 IBM 7090 computer words. The buffer memory is a Telemeter Magnetics Type 1092-BQ-8A. The magnetic tape recorder is a 7-track Potter Model 905. The control unit is programmed via a patch board allowing flexible use of the various input–output capabilities. The paper tape reading system utilizes an optical reader with a speed of 300 or 600 characters/sec. The paper tape punch is a teletype 60-character/sec punch. Power requirements for the system are 60-cycle, 115-volt AC, and 10 amperes.
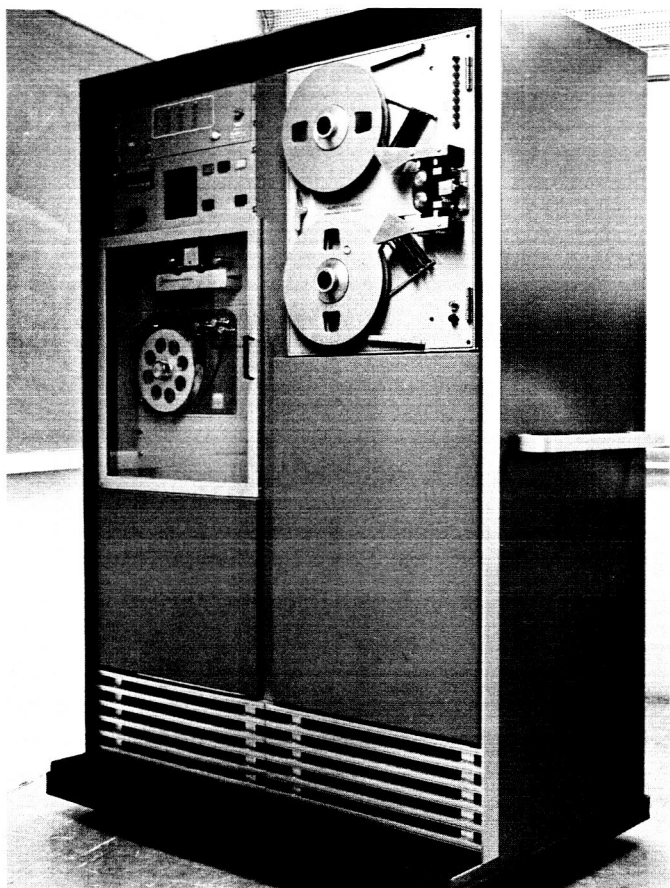
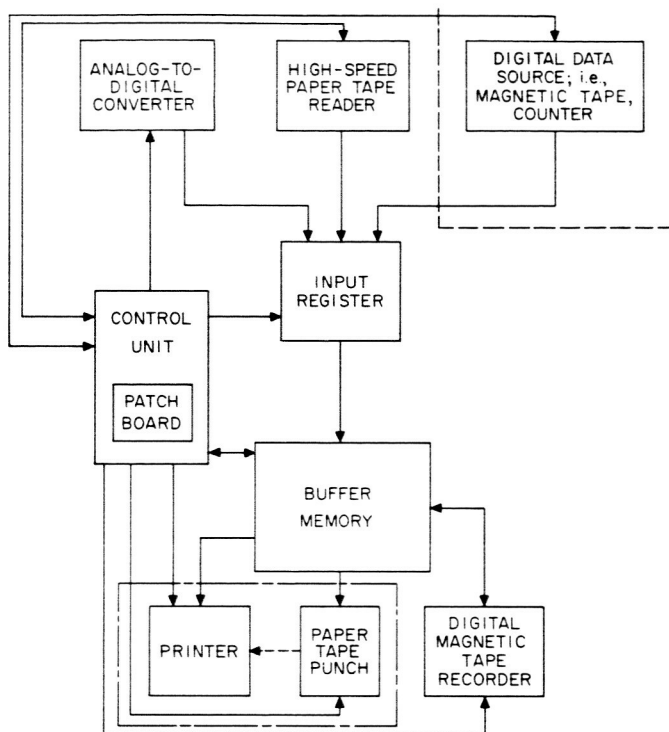Figure 17. General purpose digital data logger

Figure 18. Digilog data system

A limited amount of quick-look printing capability is planned which will allow on-site monitoring of the recording; however, full printing of raw data will not be possible without utilizing the IBM 7090 computer.

V. Engineering Research

A. Temperature Control

An analytic study to outline the basic nature of the temperature control problem that may arise in space was recently carried out. The sources of heat considered are the incident radiation from two natural sources, the stars and the Sun, and from one artificial source, a nuclear reactor.

As a representative geometry, a solid passive cube (1 foot on a side) was considered subjected to radiation from each source. An equilibrium temperature was then defined as that temperature at which the surface would stabilize in order to radiate heat at the same rate as the incoming heat. The target cube was assumed to have infinite thermal conductivity and, thus, is at a uniform temperature.

The material specifications for the target were of a more specific nature. They were selected as those which might be used in constructing a proposed cryogenic computing device. The materials were 40% glass, 50% phenyl plastic, 5% copper, and a 5% combination of tin and lead. While this blend provides a good example of the technique needed to compute combined energy absorption coefficients in the case of the penetrating radiations, it does limit the generality of the material selection. The calculations that were made can be easily modified to include almost any solid substance (or mixture, if an average density and atomic number is computed), in the case of the natural radiations, but the problem would have to be reworked for a change in percentages of components subjected to nuclear reactor radiation.

Each of the sources has associated with it an electromagnetic mode of radiation and an ionized particle mode. From the extra-solar source, the electromagnetic radiation appears to be somewhat concentrated in the galactic plane as might be expected. The extra-solar particle radiation (galactic primary cosmic rays), is composed of a range of ionized atoms which range in atomic number from 1 to about 26, of which roughly 90% are protons. Their direction of incidence appears to be uniformly distributed from all directions. The intensity of this radiation is practically time independent except for local magnetic effects, such as occur in the solar system.

The electromagnetic radiation from the Sun is directed radially outward, and the intensity follows the inverse-square law. Solar particle radiation is the same in composition as the galactic primary cosmic rays, but the direction, energy, and time variance are not accurately known. There appears to be a quiet-day intensity that consists of low-energy particles which move more or less radially outward from the direction of the Sun, though there is some doubt that this exists. If it does exist, the appearance of Sun bursts (solar storms) then increases its intensity by a thousandfold. Fairly strong magnetic fields appear to be associated with the particle emissions, and in the vicinity of 1 astronomical unit from the Sun, give to this storm an isotropically incident characteristic similar to the galactic rays. The rate of energy decay of a proton as it passes through matter is roughly inversely proportional to its energy. The galactic particles, possessing high energy, leave only a small amount of their energy in the target, while the solar protons, whatever their distributions eventually turn out to be, lose their energy in a few centimeters of material.

The reactor radiation consists of gamma rays and neutrons which are not absorbed within the shielding. The target is assumed to *see* the reactor as a point source with both modes of radiation being radially emitted. Both radiations, which lose energy exponentially in passing through matter, were assumed energetically monochromatic at 2 mev per neutron and per gamma ray. Specifically, in the geometry considered, the target was placed 30 feet away from the reactor which generated 300 kilowatts (thermal energy), and a 250-pound lithium hydride shield was located between the reactor and the target.

In obtaining the surface emissivity for thermal radiation of the cube, two problems are encountered. First, coefficients of emissivity as a function of wavelength are not well known in the far infrared, and second, very little is known about emissivity of a surface which is at extremely low temperature. It is, therefore, necessary to extrapolate available data both to longer wavelengths and to lower temperatures. For a body at very low temperature, the peak in the emission spectrum and, thus, the major portion of the emitted energy, is in the far infrared. For these reasons, it is not possible at this time to predict accurately the surface emissivity at low temperatures. However, from the available data, it appears that some materials, especially nonmetals, probably have high emissivities at low temperature. For this reason, an emissivity of 1.0 is used as representative.

Incident thermal electromagnetic radiation is in a wavelength region for which the surface absorptivity is well defined. Therefore, the principal uncertainty concerning the absorptivity coefficient is the effect of decreasing the surface temperature far below those usually maintained in making measurements. In the absence of more definitive data, this latter effect has been assumed small. Extrapolating available data and assuming that emissivity and absorptivity do not drastically change as temperature decreases, the range given in Table 9 was obtained for the equilibrium temperature of the cube in starlight.

The equilibrium temperatures and the corresponding assumed flux densities for the cubic foot of target material are given for each mode of radiation from each of the three sources in the table.

In this discussion, Table 9 is interpreted on the basis of attempting to establish cryogenic temperatures. The most obvious problem is due to the solar source. In the case of the electromagnetic mode, the problem is to thermally shield a very cold body from a very hot one. This is theoretically possible, but may prove impractical, depending on the desired temperature for the cold body.

Table 9. Equilibrium temperatures of solid cube 1 foot on a side irradiated by Sun, reactor, and extra-solar sources

Source	Temperature, °K		Assumed particle flux
	Electro-magnetic	Particle	
Solar (one astronomical unit from Sun)	250	6.7 (quiet day)	30 protons/cm³ with velocity of 2000 km/sec
		250 (storm)	$N(E) \approx 10^{18} \times E^{-5}$ $N(E) \sim$ protons/cm² sec mev $E \sim$ mev
Reactor	45 (gammas)	4.5 (neutrons)	Gammas $\sim 1.5 \times 10^{7}$ rads/year Neutrons $\sim 1.5 \times 10^{2}$ nvt
Extra-solar	10 to 20	2.7	$N(>E) \approx \dfrac{3.8 \times 10^{5}}{(1 + E)^{1.5}}$ $N \sim$ protons/m² sec ster $E \sim$ bev

For example, to thermally shield a 10°K body at 1 AU from the Sun may require as many as 10^4 radiation shields. On the other hand, if the configuration factor can be made very small, the number of shields may be appreciably reduced. This latter consideration suggests that cryogenic devices be made in the shape of rods or thin plates, thus providing little exposed area. At greater distances from the Sun, the shielding problem becomes less severe. Of course, if thermal shielding should prove impractical, active devices can be employed. The inherent transient nature of the solar proton flux during storms suggests two approaches to operation at cryogenic temperatures; either the system can operate intermittently so that it is inoperative during the storms, or a combination thermal insulation and heat capacity might be used to damp out the temperature peaks.

In connection with the reactor, the neutron component is quite effectively shielded, but the gamma ray flux which penetrates the shield is still substantial. The practical means of minimizing the gamma radiation is to move away from the reactor core and to maintain the surface-area-to-volume ratio as large as possible. The thermal radiator associated with the reactor and the reactor shield which is a thermal radiator due to the absorption of reactor radiations, create essentially the same problem as the solar electromagnetic radiation.

It is apparent that the radiation modes must have a definite directional characteristic or a time dependency if their absorption is to be minimized. Since both of the extra-solar modes are omnidirectional and time independent, the following approach appears the most promising: In order to minimize the equilibrium temperature due to particle irradiation, the surface-to-volume ratio should be as large as possible; an example of this is a

sheet configuration. With respect to the electromagnetic radiation, the surface's absorptivity should be low, relative to the emissivity at the long wavelengths.

B. Pressure Vessel Analysis

The present effort in pressure vessel analysis is directed toward the development of a complete solution for symmetrically loaded tanks with variable thickness segments. The test program of the tanks described in *RS 36-4* is continuing with the aim of correlating test results with analytical results. Two approaches are being studied with respect to the analytical solutions. First, approximate analytical solutions are being developed for the various shell segments involved (Refs 8 to 14). Second, the feasibility of programming the exact thin-shell differential equations for solution by an IBM 7090 computer is being studied.

C. Plasma Containment

Subsequent to *Research Summary No. 36-4*, it has been shown that the crucial confinement problem is in the axial direction. In a collision dominated plasma, the mechanism of confinement is quite different from the collisionless case. It has been shown that the presence of a trapped magnetic field within the plasma inhibits axial losses from a magnetic mirror (Ref 15). The magnitude of this field and some related properties can be estimated by considering the magnetohydrodynamic equations. Two postulates follow:

(1) A fully ionized, collision dominated plasma in cylindrical geometry, symmetric in azimuthal angle ϕ, and having a length-to-diameter ratio (L/D) much greater than one.

(2) There is a time-increasing external magnetic field only in the axial direction z.

The time varying external magnetic field H induces an internal electric field E in the plasma through

$$(\nabla \times \mathbf{E})_i = \mu \left(\frac{\partial \mathbf{H}}{\partial t}\right)_e \tag{1}$$

where μ is the permeability, t the time, and i and e refer to quantities interior and exterior to the plasma. Now

$$\left(\frac{\partial \mathbf{H}}{\partial t}\right)_e = \left(\frac{\partial H_z}{\partial t}\right)_e \mathbf{a}_z \tag{2}$$

from Postulate 2.

In this case, (1) becomes

$$\left[\frac{1}{r}\left(\frac{\partial}{\partial r}(rE_\phi) + \frac{\partial (E_r)}{\partial \phi}\right)\right]_i \mathbf{a}_z = \mu \left(\frac{\partial H_z}{\partial t}\right)_e \mathbf{a}_z \tag{3}$$

where r is the radial coordinate.

From symmetry

$$\frac{\partial}{\partial \phi}(E_r) = 0 \tag{4}$$

and then

$$\left(\frac{1}{r}\frac{\partial}{\partial r}(r E_\phi)\right)_i = \mu \left(\frac{\partial H_z}{\partial t}\right)_e \tag{5}$$

The azimuthal electric field gives rise to an azimuthal current density, j_ϕ, by

$$(j_\phi)_i = (\sigma E_\phi)_i \tag{6}$$

where σ is the electrical conductivity, provided the plasma is stationary. This current in turn produces an internal magnetic field, which is given by

$$(\nabla \times \mathbf{H})_i = (4\pi j_\phi)_i \tag{7}$$

or equating components

$$\left(\frac{\partial H_r}{\partial z} - \frac{\partial H_z}{\partial r}\right)_i = (4\pi j_\phi)_i \tag{8}$$

For

$$(L/D) > 1, \frac{\partial H_r}{\partial z} \approx 0$$

and

$$\left(-\frac{\partial H_z}{\partial r}\right)_i = (4\pi j_\phi)_i \tag{9}$$

Now, if the rise time of the external magnetic field is quite short, the induced current density will fall to zero over a short time. Then

$$-\left(\frac{\partial H_z}{\partial r}\right)_i = 0 \qquad (10)$$

$$(H_z)_i = \text{constant} \qquad (11)$$

One must now consider the decay of this field in time, or

$$\left(\frac{\partial H}{\partial t}\right)_i = \left(\nabla \times \left[\mathbf{v} \times \mathbf{H} - \frac{\mathbf{j}}{\mu\sigma}\right]\right)_i \qquad (12)$$

where $\mathbf{v}$ is the plasma velocity and is zero for a stationary plasma. But

$$\mathbf{j} = \frac{1}{4\pi} \nabla \times \mathbf{H} \qquad (13)$$

If $\eta = (4\pi\mu\sigma)^{-1}$ then (12) becomes

$$\left(\frac{\partial H}{\partial t}\right)_i = (\eta \nabla^2 H)_i \qquad (14)$$

Thus, one sees that the interior magnetic field "leaks" through the material from point to point with time. This decay time for a spherical plasma is

$$t_d = \pi\mu\sigma D^2 \qquad (15)$$

to within an order of magnitude (Ref 16). This then sets the maximum confinement time in the axial direction. Note that if the plasma begins to diffuse radially through the internal z-direction magnetic field

$$\left(\frac{\partial H}{\partial t}\right)_i = (\eta \nabla^2 H + \nabla \times \mathbf{v} \times \mathbf{H})_i \qquad (16)$$

The $\mathbf{v} \times \mathbf{H}$ term gives rise to an azimuthal force which tends to rotate the entire plasma. Experiments which have been carried out at the Naval Research Laboratory have shown that a rotation of the plasma does take place under the conditions postulated. This suggests that the observed rotation may be due to leakage of the plasma through the internal field lines.

ENGINEERING FACILITIES DIVISION

VI. Wind Tunnel and Environmental Facilities

A. 20-Inch Supersonic Wind Tunnel

1. Tunnel Development Program

A complete recalibration of the air flow field in the 20-inch supersonic wind tunnel has been performed (Test 20-C36). The portion of the test rhombus which was calibrated extended from a point 36.5 inches upstream from the center of the test-section window to a point 11.5 inches downstream from the window. Models are normally installed within the window area to facilitate visual and optical observations. The test section is 20 inches high and 18 inches wide.

The axial pitot pressure distribution was measured with a three-tube rake mounted on a motor-driven support as shown in Figure 19. This rake with its pitot tubes mounted on 3-inch centers could be rolled by remote control and, thus, the flow could be easily inspected on the tunnel centerline as well as 3 and 6 inches above, below, and on both sides of the centerline. A pair of pitot tubes was mounted on a vertical traverse in the vertical centerline plane of the tunnel at the center of the window (sta −20.00) to establish the absolute levels of the pitot pressures measured by the axial traverse. The pitot pressures were sensed by transducers installed in the wind tunnel (to reduce lag time) and plotted directly on a JPL-developed plotting machine and a Moseley plotter. The plotting pens were driven by the transducer outputs and the plotting table movement represented axial or vertical travel of the probe.

Variations in pressure and Mach number on the tunnel centerline for nineteen calibrated Mach numbers are listed in Table 10. It has been demonstrated previously that other Mach numbers within the range can be run when necessary and provide flow quality similar to that shown in this report. The actual centerline Mach number distribution for the calibrated Mach numbers is shown in Figure 20. The small pressure bump that appears in the vicinity of station −20 at the lower Mach numbers results from the joint between the leading edge of the test section window frame and the tunnel sidewall.

Since it is planned to correct the lateral position of the windows and thus eliminate this pressure bump, the centerline Mach number and pressure variations listed in Table 10 do not include this particular disturbance. The pressure bump that occasionally appears at the downstream end of the centerline trace results from a disturbance created by the vertical traverse and is not present during ordinary model testing. A sample vertical trace is shown in Figure 21.

Table 10. Calibrated Mach numbers for 20-inch supersonic wind tunnel

| Nominal Mach No.	Throat height, in.	Centerline mean Mach No. and variation[a]		Centerline variation			Calibration conditions	
				$\frac{\Delta p_0'}{p_0}$	$\frac{\Delta p}{p_0}$	$\frac{\Delta M}{M}$	Supply pressure, cm Hg abs	Supply temperature °F
1.33	18.18	1.333	±0.005	0.002	0.003	0.005	105	122
1.40	17.65	1.404	±0.005	0.002	0.004	0.007	110	124
1.48	17.72	1.481	±0.003	0.003	0.004	0.007	82	110
1.65	14.90	1.653	±0.005	0.003	0.003	0.005	115	113
1.81	13.24	1.814	±0.005	0.004	0.003	0.006	74	100
2.01	11.30	2.012	±0.004	0.004	0.002	0.004	74	94
2.21	9.43	2.214	±0.005	0.004	0.001	0.004	115	121
2.41	7.75	2.405	±0.005	0.004	0.001	0.004	105	109
2.61	6.40	2.610	±0.005	0.004	0.001	0.003	125	111
2.81	5.30	2.812	±0.004	0.003	0.0004	0.003	145	108
3.01	4.40	3.010	±0.006	0.003	0.0004	0.003	150	109
3.26	3.44	3.262	±0.003	0.002	0.0003	0.002	155	115
3.50	2.70	3.503	±0.005	0.002	0.0002	0.003	190	143
3.74	2.12	3.742	±0.008	0.002	0.0002	0.003	215	124
3.99	1.70	3.989	±0.006	0.003	0.0001	0.004	255	121
4.24	1.32	4.239	±0.006	0.003	0.00005	0.004	300	143
4.54	1.04	4.544	±0.006	0.001	0.00005	0.004	330	121
4.76	0.91	4.762	±0.006	0.006	0.00005	0.003	330	127
5.01	0.71	5.014	±0.007	0.007	0.00003	0.003	330	155

[a]Between stations −5.0 and −25.0 in.
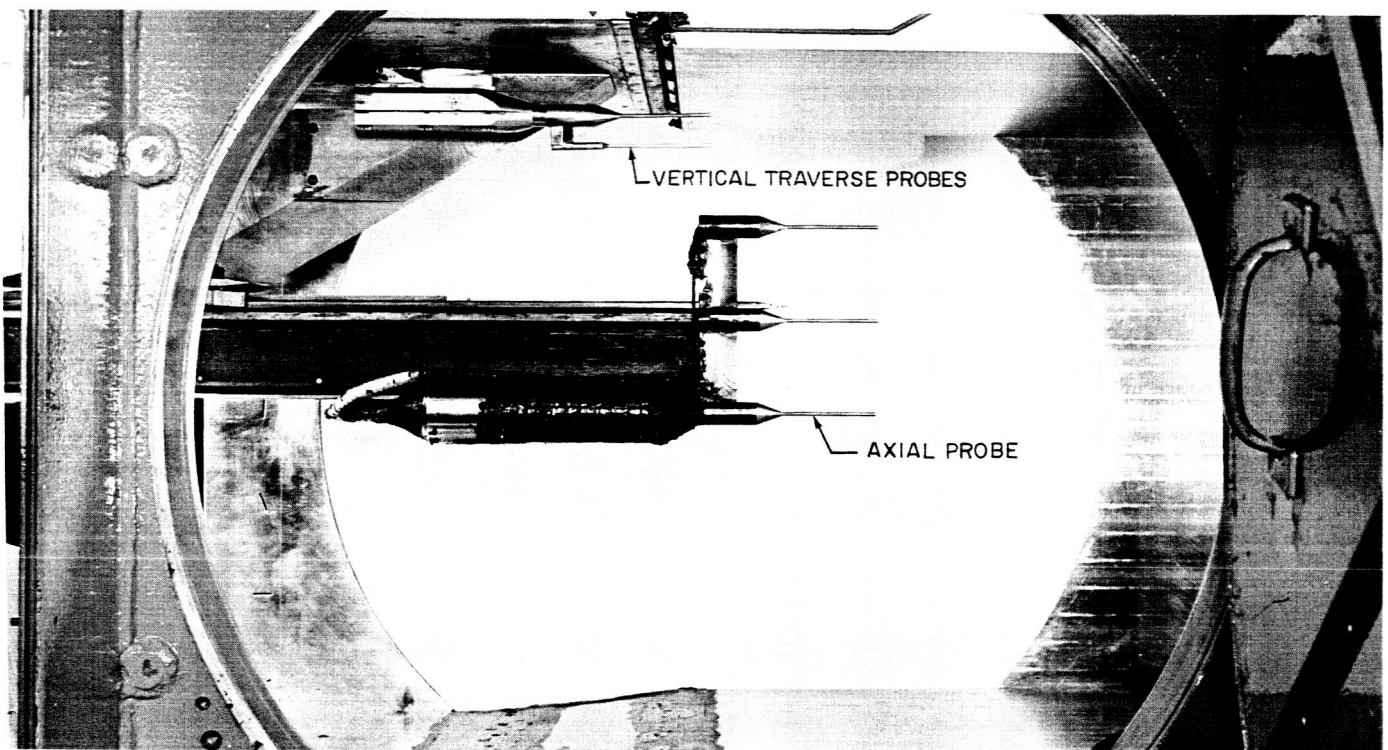
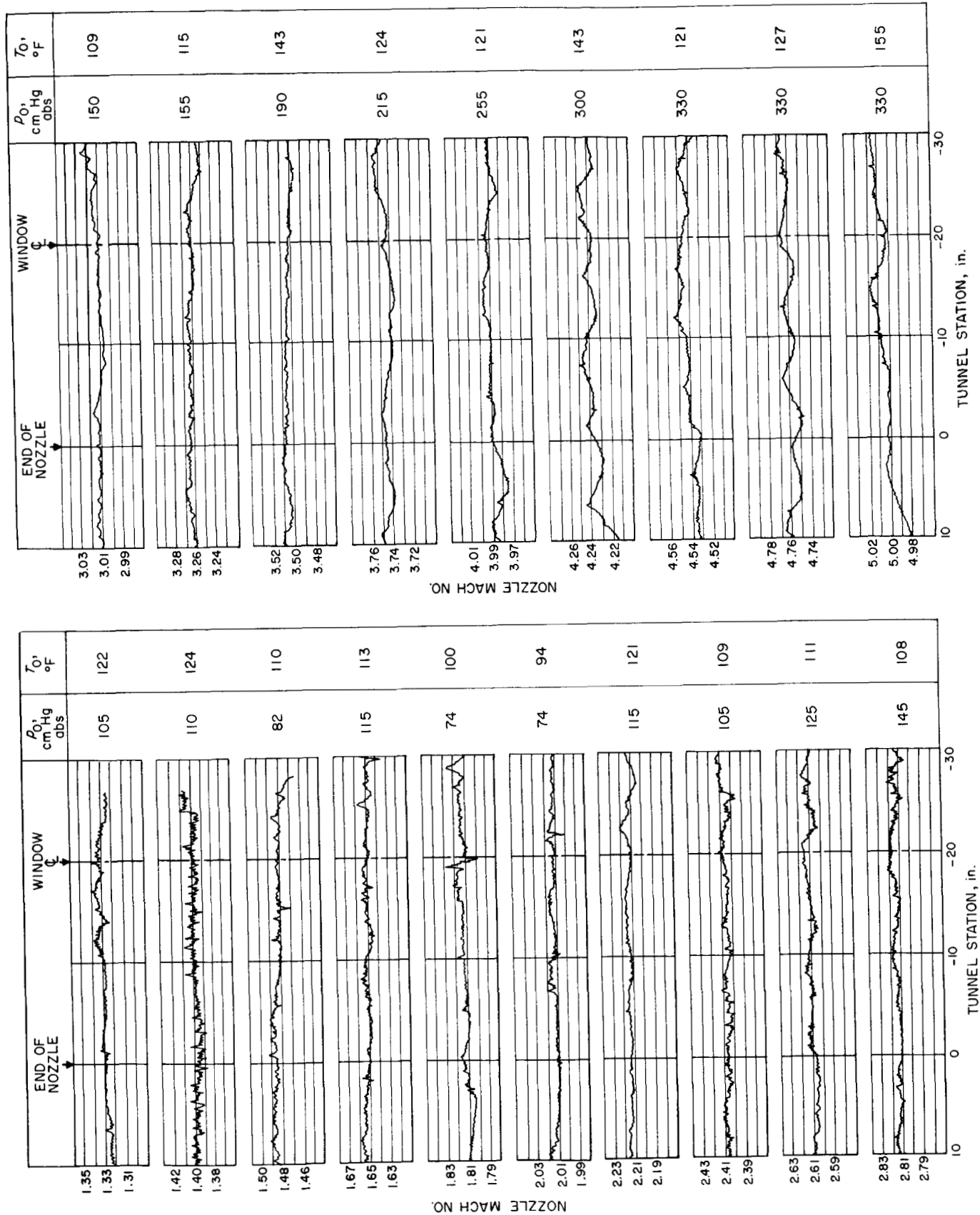Figure 19. Probes mounted in wind tunnel

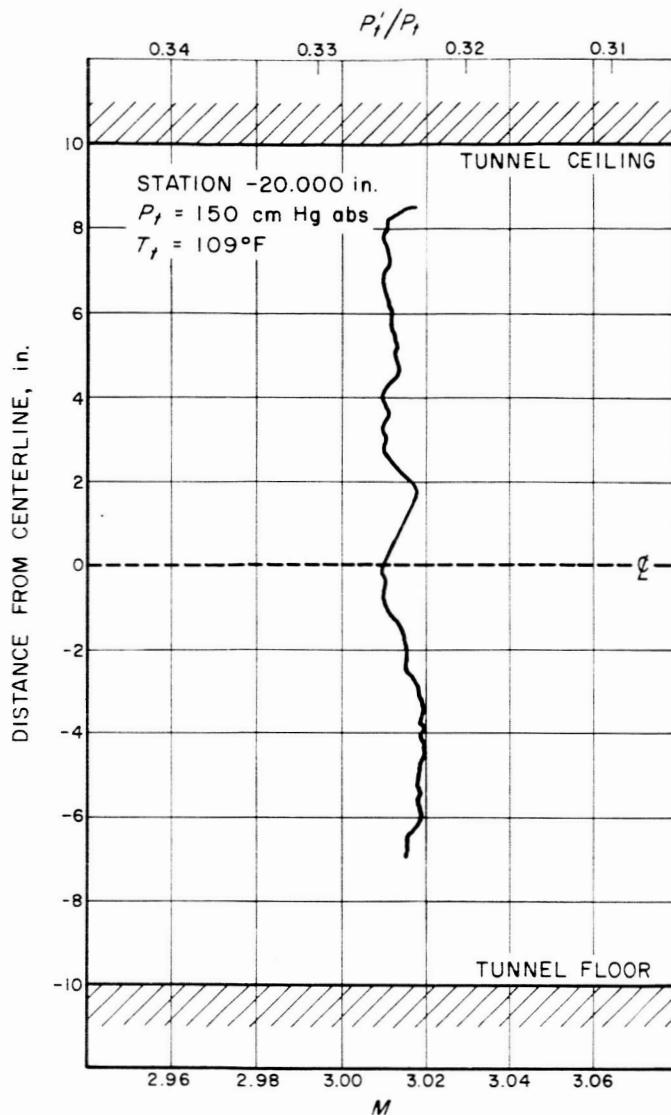Figure 20. Centerline flow calibration at various Mach numbers in the 20-inch supersonic wind tunnel

Figure 21. Vertical Mach number distribution
for $M = 3.01$

B. Environmental Facilities

1. Environmental Test Programs

Testing of the *Ranger* RA-1 proof test model (PTM) has been completed in the 6- by 7-foot space simulator. A chamber pressure of approximately 2×10^{-5} mm Hg was maintained for the test. Temperature control of the PTM was obtained by modifying the chamber nitrogen feed lines so that a mixture of gaseous and liquid nitro-

gen would circulate through the wall shrouding, maintaining an average temperature of 32°F. At the start of the test, the Earth sensor exceeded the upper temperature limit. Therefore, the component was provided with individual temperature control by mounting the sensor on a plate cooled by an external cooling device, which successfully maintained the temperature of the sensor within its limits for the remainder of the test. After 3 days, the PTM temperature conditions stabilized, and the tests continued under these conditions for 10 days. The space simulator (at atmospheric temperature) was used for PTM temperature tests, since the existing instrumentation cables were too short to allow the test to be performed in a temperature chamber without moving much instrumentation, with consequent loss of time. Temperatures of 32, 86, and 122°F were held for a period of 24 hours each, after stabilization. During these tests, a maximum variation of temperature recorded was ±2°F.

Testing of the RA-1 temperature control model (Fig 22) shows the model prior to a test. During these temperature control tests, the wall shrouding was cooled by liquid nitrogen to −320°F and the pressure was held near 2×10^{-5} mm Hg.
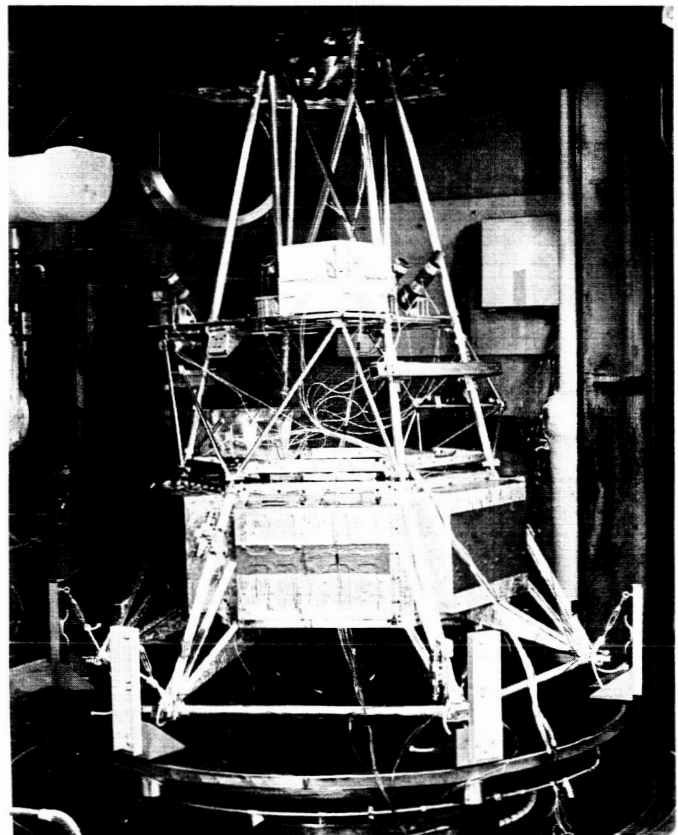

Figure 22. *Ranger* RA-1 temperature control model

2. Test Equipment Development

In order to improve the quality of component vibration testing in the horizontal plane, a portable oil-film table has been designed and fabricated. This table, which weighs 1200 pounds, consists of a 24- by 24- by 4-inch steel surface plate attached to a base of 8-inch-square steel tubing. Four casters are attached to the base to give the table the necessary mobility to move from one shaker or system to another. Three hydraulic jacks operating in an inverted position provide the table with the necessary leveling ability. By using either of two different sized surface plates, the table can be used with the 1200-pound shakers, or with 5000- and 7000-pound shakers. Figure 23 shows the table set up for use with a 1200-pound shaker. Evaluation tests were run to compare the dynamic characteristics of the oil-film table with those of a right-angle adapter. In Figure 24, the vertical cross coupling acceleration is plotted against the test acceleration; i.e., acceleration parallel to the motion of the exciter head. The oil-film table is shown to be far superior to the right-angle adapter. With the right-angle adapter the acceleration ratio is just less than 1-to-1; with the oil-film table, the ratio is about 1-to-6. In the future it is expected that all of the high-frequency vibration testing in the horizontal planes will be done on an oil-film table.

This report period witnessed the initiation of an extensive experimental and building program leading toward the duplica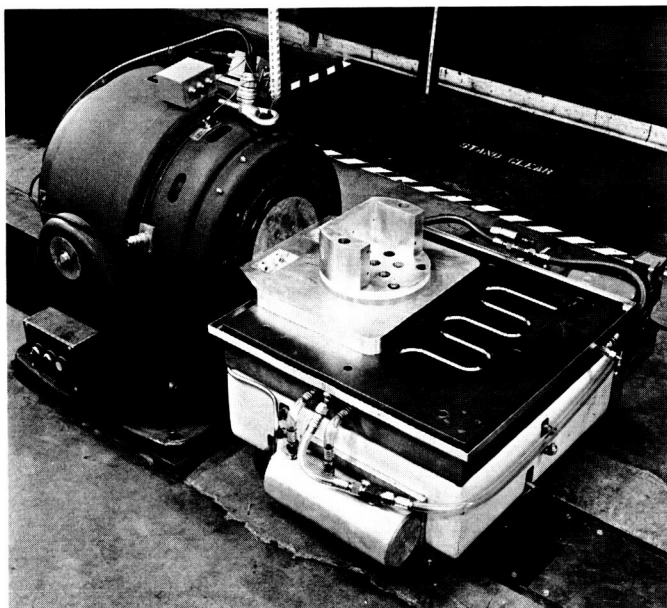tion of space environments at JPL. The Laboratory now has a contract with Consolidated Vacuum Corporation, Rochester, New York, to design and build a large space simulator for testing complete lunar and planetary spacecraft. The pressure vessel will be 27 feet in diameter by about 52 feet high with an effective testing volume of 25 feet in diameter. It will simulate the cold of space with black LN_2 panels which completely cover the insides of the tank; simulate the vacuum of space by being able to continuously maintain a pressure of 10^{-6} mm Hg; and simulate the effects of solar radiation by illuminating a 15-foot diameter circle with uniform ($\pm10\%$), parallel (±4.5 deg) light at any intensity between half and twice that of the Earth solar constant. This facility will represent a major advance in the state of the art of environmental testing and promises to be of primary importance in the reliability testing of complete systems. The facility construction is currently scheduled to be finished in November 1961.

Experimental work in radiation sources, optical components, measurements and systems has been initiated with the fourfold purpose of complementing the solar simulation capability of the large simulator, developing adequate measurement techniques, producing smaller simulators adequate for laboratory work, and developing the Laboratory's capabilities in this field.
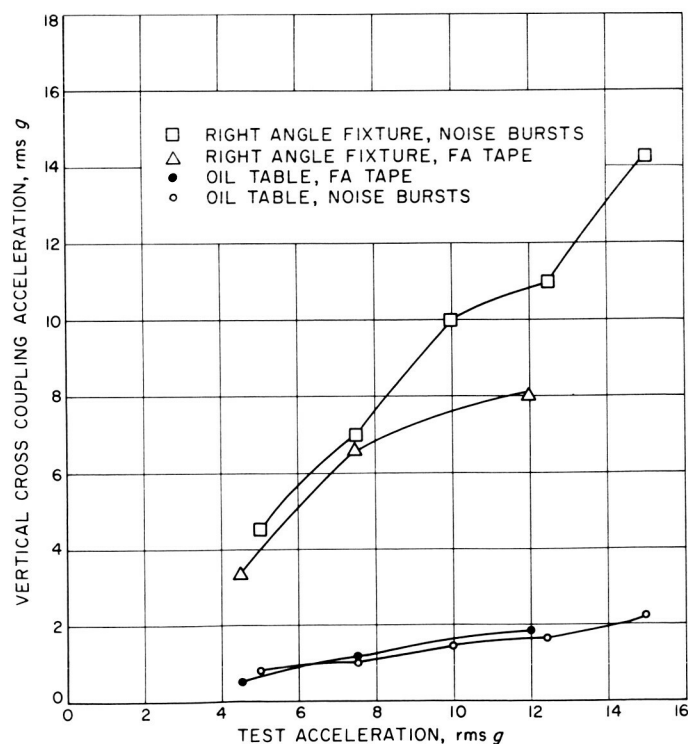

Figure 23. Portable oil-film shake test table

Figure 24. Cross coupling vs input acceleration

C. Compressor Plant

1. Compressors

This report period was marked by the completion of three long-range programs for extending the operational range of the wind tunnels.

First, the existing seven large centrifugal blowers, which have been utilized in a four-stage combination to run the 20-inch SWT up to Mach 5, have been restaged through suitable valving to produce a five-stage compressor plant capable of powering the tunnel up to a Mach number of 6. Increased air temperature necessary for higher Mach number operation is provided by utilizing the heat of compression with a bypass around the aftercooler of the last stage compressor.

Second, to accommodate an increasing number of test programs which utilize gas jets from within the model to provide control forces, a high-pressure regulated gaseous nitrogen supply line has been provided to the test sections of both the 20-inch SWT and the 21-inch HWT. This line is capable of on-off control while providing weight flows up to 8 lb/sec of GN_2 at pressures up to 1000 psi.

Third, to provide supersonic testing capacity at lowest possible Reynolds numbers, a two-stage 500-horsepower Ingersoll-Rand Axi-Compressor has been installed for use as a vacuum pump for the 20-inch SWT and nearby test pits. Initial tunnel operation has been successful at supply pressures below 5 cm Hg absolute, while the tunnel flow has remained smooth and free of obvious fluctuations.

PROPULSION DIVISION

VII. Liquid Propellant Propulsion

A. Propulsion Systems

1. Cryogenic Propulsion Systems

The efficient performance of current and possible future space exploration missions, with their difficult trajectory and payload requirements, depends on the availability and use of propulsion equipment having increasingly higher performance (exhaust velocity).

The High-Energy Liquid Propellant Research Program has up to now been concerned with *storable* liquid propellants such as N_2O_4-N_2H_4 and ClF_3-N_2H_4 having theoretical exhaust velocities of approximately 8300 ft/sec (expanding to 14.7 psia from 300 psia chamber pressure). Liquid propellant systems using oxygen or fluorine as the oxidizer and hydrogen as the fuel have a theoretical exhaust velocity in excess of 11,000 ft/sec. Various preliminary design studies indicate that the insulation requirements associated with the use of these cryogenic propellants can, for most missions, be satisfied without appreciably depleting the performance advantage these propellants have over the *storable* liquid propellants. Further, the large tank volume required for the low-density liquid hydrogen is not a limiting factor in upper-stage vehicles, although it might be a limiting factor if the hydrogen were used as the fuel in a first-stage booster.

Beyond the performance limits of chemical reaction rocket motors, exhaust velocities of 20,000 on up to 640,000 ft/sec are expected to be obtained using, respectively, hydrogen heated in a nuclear reactor, electrically heated working fluids, plasma jets, and finally, ion expulsion devices. Cryogenic working fluids will be used in many of these propulsion systems.

Because of the above considerations, the High-Energy Liquid Propellant Research Program has been reoriented and renamed the Cryogenic Propulsion Systems Program. The stand at the Edwards Test Station which had been used for the recently completed ClF_3-N_2H_4 program is being modified to utilize cryogenic propellants.

The multiple objectives of the Cryogenic Propulsion Systems Program are:

(1) To achieve an understanding of the properties of the cryogenic fluids, especially oxygen and hydrogen, and of the requirements imposed by these properties on the materials and equipment used with these fluids.

(2) To develop a competence in the handling, storage, and transfer of the cryogenic fluids, and in the design, fabrication, and operation of components used with the cryogenic fluids.

(3) To obtain experience in the design and operation of LO_2–LH_2 rocket motor systems in order to provide test and evaluation ability and engineering capability necessary for considering cryogenic propulsion systems in future JPL spacecraft programs.

The program will start with the installation of cryogenic storage tanks and test station equipment which will enable experience to be obtained in the handling of the cryogenic propellants and in the operation of the components in cryogenic systems. Engine problems, which are at the heart of propulsion system development, will be investigated next. These include the areas of combustion chamber fabrication, injector design and fabrication, performance, combustion stability, and heat-transfer and cooling. As soon as possible, the program will be broadened to simulate and solve problems which would arise in the design and operation of complete propulsion systems and vehicle stages using cryogenic propellants. These problems include fluid metering devices and propellant utilization systems, instrumentation, ground handling and loading, insulation requirements, and flight-weight component development.

The information obtained and the experience gained in pursuing the above objectives will be of value in programs wherein the Jet Propulsion Laboratory may be called upon to design, fabricate, and operate a high-performance vehicle or stage, or to monitor the design, fabrication, and operation of such a vehicle or stage by industrial contractors.

B. Combustion and Injection

1. Rocket Motor Injection Research

The experimental performance of the RMIR Injector 7 injecting $N_2O_4 + N_2H_4$ into a 40-inch L^* chamber was presented in RS 36-6, Volume II. Since the performance levels achieved in those tests were relatively high (i.e., 96 to 97% c^*_{th}), and since it is expected that the high reaction rates attributable to this propellant system would require a minimum combustion volume, the performance
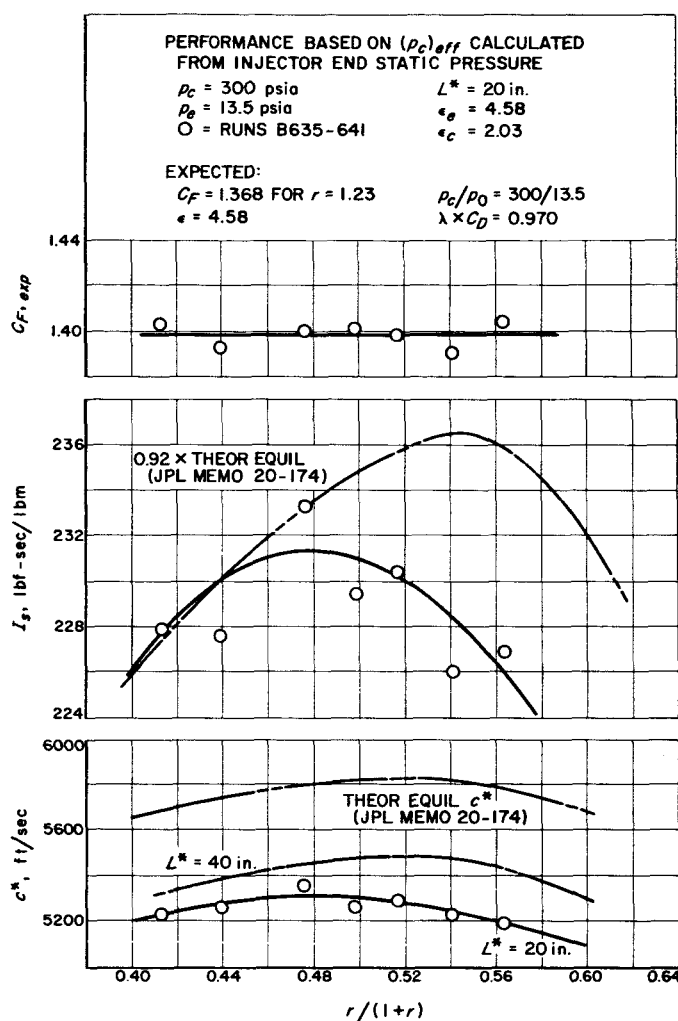

Figure 25. Experimental performance of Injector D-9111607 Mod 1 (Injector 7) with $N_2O_4 + N_2H_4$

for this injector-propellant combination was evaluated in a significantly smaller combustion chamber. This was accomplished with a chamber having the same diameter as the 40-inch L^* chamber but which is approximately one-half as long in order to give an L^* of 20 inches. The results of these tests are shown in Figure 25 which compares I_s, c^*, and C_F with theoretical performance over a range of mixture ratios.

By comparing these data to those obtained in the 40-inch chamber (RS 36-6, Vol II), it can be seen that the general performance characteristics are similar but that the absolute level is significantly lower—i.e., a decrease of approximately 4% in both c^* and I_s—and that peak performance mixture ratio is lower for the smaller L^*. It is interesting to note that a shift in peak performance mixture ratio to a somewhat lower value as seen here was also observed for Injector 5 with *Corporal*

propellants (RS 5). Although it is obvious that these two sets of data do not in themselves define the limiting combustion length, it is reasonably certain that they have bracketed the optimum length for this engine configuration.

It should be particularly noted that the c^* values presented here are calculated from the effective chamber pressure as determined from a measurement obtained at the injector end of the combustion chamber, and that this is not the measurement that is usually used when reporting c^*. Therefore, in order to obtain a direct comparison between the 20-inch L^* and the 40-inch L^* chambers, Figure 25 also includes a plot of c^* vs $r/(1 + r)$ for the 40-inch chamber calculated from injector-end chamber pressure. It is seen that the incremental degradation of performance with chamber length is essentially the same as was observed with I_s, although the absolute level of c^* is still questionable.

With regard to this change in the choice of a pressure measurement from which c^* is calculated, it can only be reiterated that the determination of the nozzle inlet stagnation pressure becomes increasingly difficult as chamber length decreases. As was noted in RS 5, the discrepancy in this determination for Injector 5 with *Corporal* propellants increased from 2.5% to 9.6% as L^* changed from 40 inches to 20 inches; whereas for Injector 7 with N_2O_4–N_2H_4 propellants, the discrepancy increased from approximately 2% to 7% as the L^* changed from 40 inches to 20 inches. This phenomenon is particularly disconcerting since c^* based on the nozzle inlet static pressure measurement (which involves fewer assumptions than the comparable injector end measurement) tends to *increase* (or at least remain nearly constant) as combustion length decreases and, therefore, is completely inconsistent with performance based on thrust measurements. Thus, it is concluded that the best comparison of performance is obtained from thrust data and that the near-ideal conditions postulated for the one-dimensional model used to derive the equations for total pressure in the chamber (Ref 17) must be satisfied if c^* is to be a significant measure of performance.

Finally, it is observed that the degradation in performance level for this propellant-injector combination as L^* decreases is somewhat less than was observed with *Corporal* propellants and RMIR Injector 5 (RS 5). For example, the peak performance decrement for I_s with Injector 7 with N_2O_4 + N_2H_4 was about 4% as L^* decreased from 40 inches to 20 inches, while the comparable decrement with Injector 5 with *Corporal* propellants was about 5%. For c^* (based on injector end pressure measurements) the comparable numbers are 5% and 7%, respectively.

C. Heat Transfer and Fluid Mechanics

1. Heat Transfer in Rocket Motors

An experimental investigation of heat transfer in rocket engines is being conducted to determine the effect of injector configuration, thrust-chamber geometry, and operating conditions on the axial heat flux distribution. These tests are being made at chamber pressures between 100 and 300 psia, with hydrazine (N_2H_4) and nitrogen tetroxide (N_2O_4) as bipropellants at a nominal mixture ratio of 1.0. Steady-state experimental values of heat flux are measured calorimetrically by passing cooling water through axially-short, circumferential coolant passages which form the thrust-chamber walls. Comparisons between the analytical and experimental values of local heat flux have been made with 1.64-to-1, 4-to-1, and 8-to-1 contraction-area-ratio nozzles and were reported in RS 5, RS 36-1 (Vol I), RS 36-2 (Vol I, Part Two), RS 36-4 (Vol II), RS 36-5 (Vol II), and RS 36-6 (Vol II). Analytical values of the heat-transfer coefficient have been calculated by the method proposed in Reference 18. As suggested in Reference 19, enthalpy difference between the free stream and the wall temperature condition was used as the driving potential in calculating predicted values of local heat flux.

In RS 36-6 (Vol II), heat transfer results were reported for a 4-to-1 contraction-area-ratio nozzle operating with an eight-orifice-pair Enzian type injector and a 23.7-inch L^* at chamber pressures between 99 and 265 psia. A description of the thrust chamber and injector is also reported in RS 36-6 (Vol II). In order to determine gross effects of change in L^* on heat transfer rates, four additional tests were made with the above-described configuration at an increased chamber length ($L^* = 39.7$ inches). The experimental results of these tests are compared with the analytical prediction in Figures 26 and 27. Operating conditions for each test are also noted in Figures 26 and 27.

The experimental heat flux results at low chamber pressure shown in Figure 26 are approximately 10% above, 30% below, and 35% below the predicted values for the combustion chamber, nozzle throat region, and nozzle expansion region, respectively; except for the peak experimental heat flux which occurred somewhat upstream of the geometric throat, the experimental heat fluxes for the nozzle contraction region are very near the predicted values. These results follow the trends obtained for the 23.7-inch L^* tests at low chamber pressure reported in RS 36-6 (Vol II). Experimental values of local
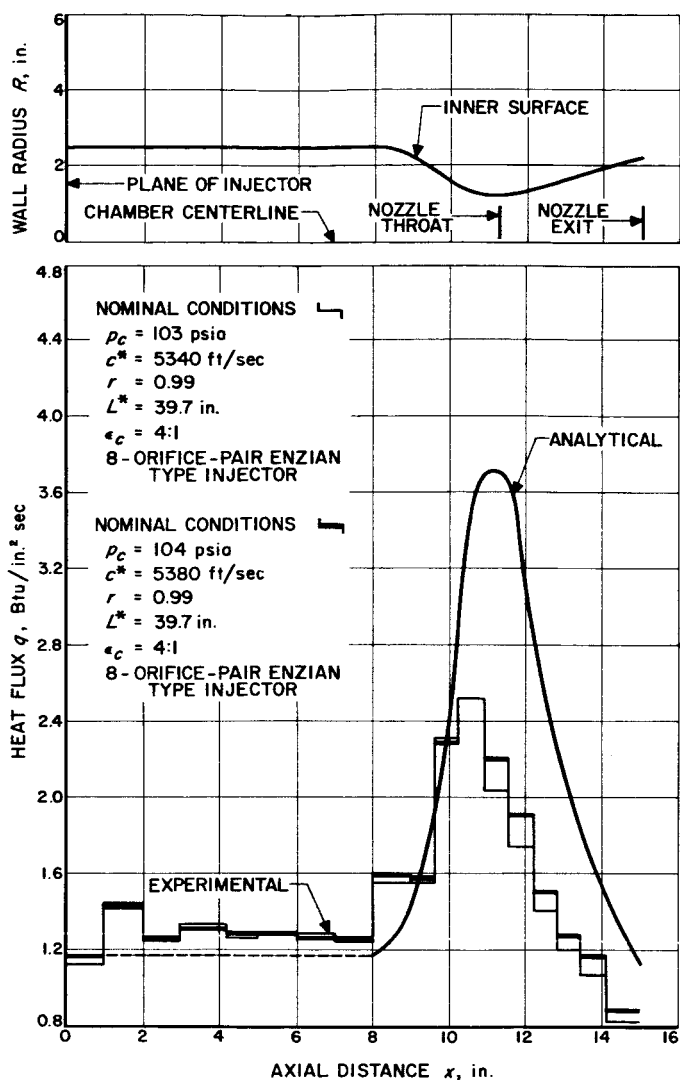
Figure 26. Comparison of analytical and experimental heat-flux distribution at low chamber pressure

shift of peak experimental heat flux, the heat flux for the nozzle contraction region was in agreement with the prediction. Two thermocouples in the nozzle expansion region read erratically throughout the test made at 278-psia chamber pressure and gave rise to apparent irregularity in the experimental heat flux curve in Figure 27. These spurious results were disregarded in making the foregoing comparisons.

In Figure 28, maximum experimental heat flux values are shown as a function of chamber pressure for both the 23.7 and 39.7-inch L^* tests. The analytical prediction for the nozzle throat is also shown in Figure 28 for purposes of comparison. Since characteristic velocity c^* was approximately 4% higher for the 39.7-inch L^* tests, both

heat flux substantially below predicted were also obtained at chamber pressures near 100 psia with the 8-to-1 contraction-area-ratio nozzle; however, good agreement between the prediction and experimental results was observed in tests made with a 1.64-to-1 contraction-area-ratio nozzle at similar operating conditions. These differences in correlation are believed to be explained by the differences in splash plate pressure drop discussed in RS 36-6 (Vol II) and differences in combustion phenomena discussed in Reference 20.

The experimental heat flux results at higher chamber pressure shown in Figure 27 are approximately 15% below, 5% above, and 20% below the predicted values for the combustion chamber, nozzle throat region, and nozzle expansion region, respectively; except for the upstream
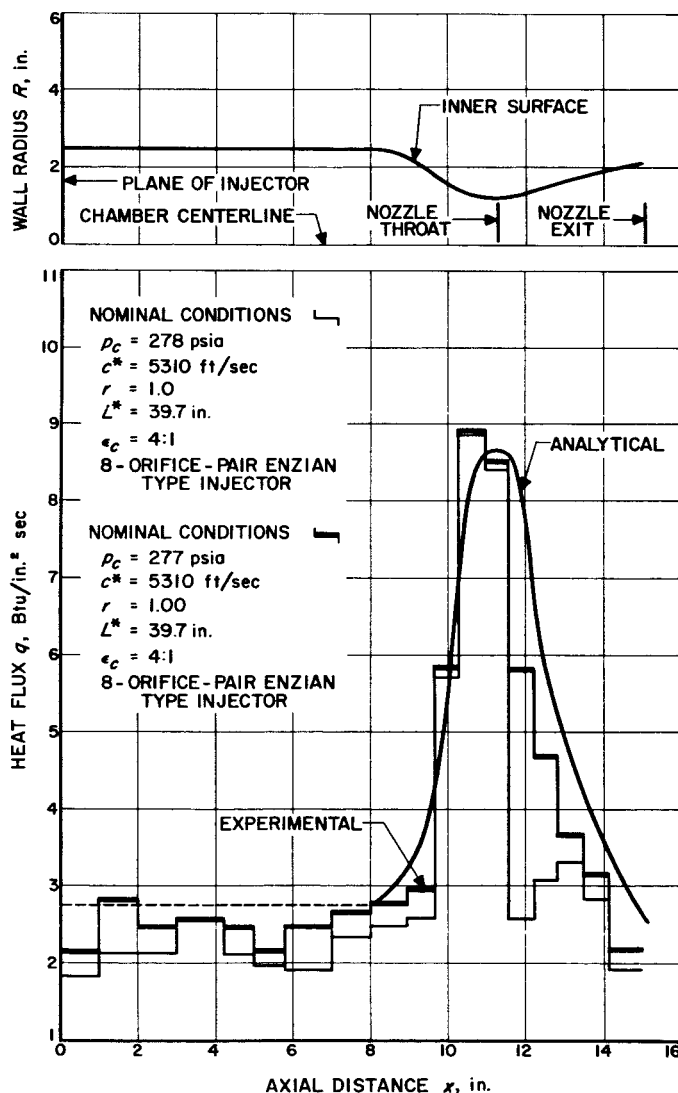

Figure 27. Comparison of analytical and experimental heat-flux distribution at high chamber pressure
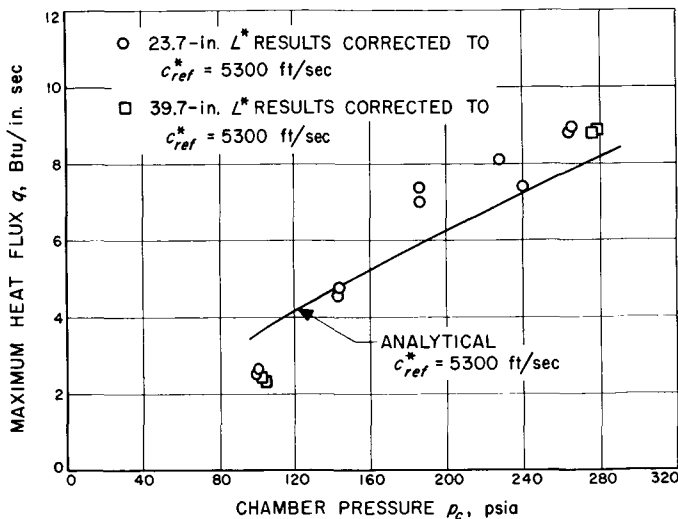
Figure 28. Maximum heat flux as a function of chamber pressure

the predicted and the experimental values of heat flux were corrected to a reference c^* of 5300 ft/sec for the basis of comparison. The increase in performance of the 39.7-inch L^* tests is presumably the result of increased combustion chamber length.

Thus, the results of these additional tests with the 4-to-1 nozzle at 39.7-inch L^* compared with the 23.7-inch L^* results of *RS 36-6* (Vol II) indicate that, other than the usual increase of heat transfer due to increased c^*, no apparent changes in local heat flux occur for this L^* change.

D. Propulsion Analysis

1. Mass and Performance Estimates of an Advanced Storable Liquid Propellant Propulsion System

Several propulsion system preliminary design studies are currently underway. The purpose of these investigations is to determine which propellants and propulsion systems present the greatest promise for terminal propulsion use in unmanned interplanetary spacecraft. Some typical terminal propulsion demands might be the establishment of planetary satellites and the deceleration of planetary landing packages. These missions are characterized by modest vehicle mass, small velocity addition compared with Earth escape, and long transit times from Earth.

The first of these systems to be examined was that utilizing hydrazine and nitrogen tetroxide as propellants. This particular propellant combination was selected because of its low vapor pressure, high specific impulse, and advanced state of development. Propulsion system characteristics commensurate with a 1964 flight date were assumed. The basic system concepts are illustrated schematically in Figure 29. The propellants are assumed to be stored within Teflon bladders in aluminum tanks. The products of a single hydrazine monopropellant gas generator are used to pressurize and expel both propellants. The monopropellant is stored in a helium-pressurized aluminum vessel. Pressure-operated valves have been assumed, and capability of multiple starts is included. A heat exchanger is included in the oxidizer plumbing circuit to cool the gas-generator products to 140°F before they are introduced into the propellant tanks. The thrust chamber (with $L^* = 40$ in.; see Table 11 for nomenclature) is assumed to be cooled by radiation only. Two chamber pressures (50 and 150 psia) and two chamber materials (tungsten and pyrolytic graphite) have been considered in the performance estimates. These estimates assume a successful development effort in the fields of
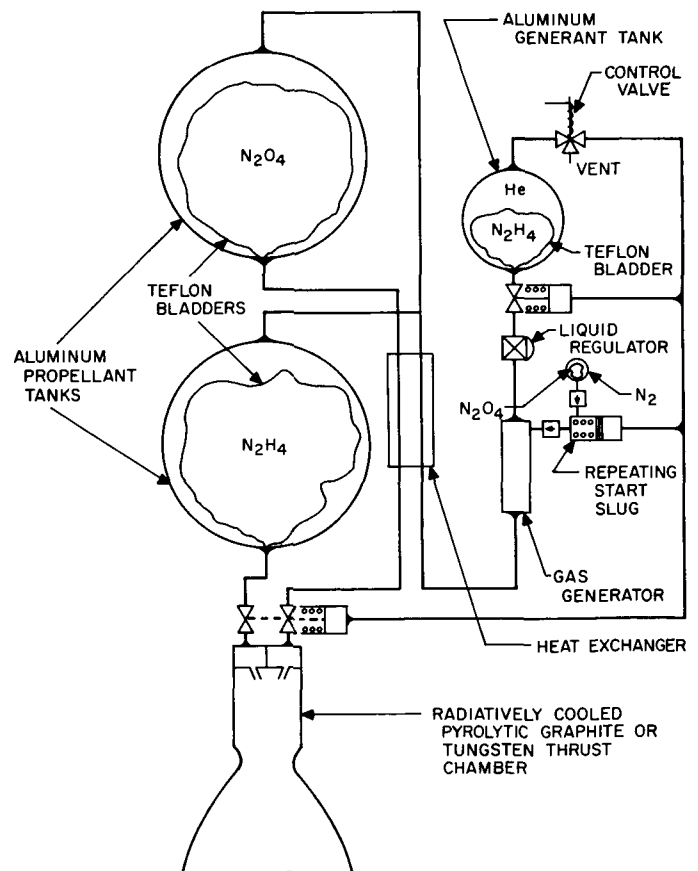

Figure 29. Advanced space-storable propulsion system

Table 11. Nomenclature

F	= vacuum thrust
I_s	= vacuum specific impulse
p_c	= chamber pressure
ΔV	= free-space vacuum velocity increment
V_h	= hyperbolic excess velocity
M_p	= propellant mass
M_{pa}	= propulsion system mass
M_s	= propellant-scaled propulsion system mass
M_f	= thrust-scaled propulsion system mass
ϵ	= expansion ratio

thrust chamber fabrication, propellant tankage, and tank bladders. Detailed information concerning the system is presented in Table 12.

No allowance has been made for thrust vector control or for interstage structure. Envelope restrictions of the spacecraft or shroud may determine the particular thrust chamber configuration to be used. The propulsion system mass estimates were based upon separate tanks for the two propellants. Recent studies have shown that the mass of a single integral tank and its accompanying structure is approximately the same as that of two separate tanks for the propellant volume and tank pressure ranges of interest.

Based upon the preceding assumptions, mass estimates of the inert components of the propulsion system were

Table 12. Example retro-rocket specifications

Specification	Value
Gross mass at ignition, lb	5000
Free-space vacuum velocity increment, ft/sec	7500
Maximum storage time in space, days	240
Gravity burning-time loss, ft/sec	20
Total effective velocity increment, ft/sec	7520
Vacuum thrust, lb	4000
Propellants	$N_2O_4-N_2H_4$
Vacuum specific impulse, lb-sec/lb	317
Propellant mass required, lb	2610
Mixture ratio, oxidizer/fuel	1.2
Combined density, lb/ft³	74.2
Thrust chamber material	Pyrolytic graphite
Thrust chamber pressure, psia	150
Expansion ratio	40:1
Propellant tank material	Aluminum
Propellant tank operating pressure, psia	225
Minimum generant tank pressure, psia	450
Initial generant tank pressure, psia	960

made. The results are presented in graphical form in Figures 30 to 34. To determine the inert propulsion system mass for a particular propellant mass and thrust level, one need only determine the propellant scaled mass fraction M_s/M_p from Figure 30 and the thrust scaled mass fraction M_f/F from Figures 31, 32, 33, or 34 depending upon the choice of engine material and chamber pressure. The inert system mass may then be determined from the following:

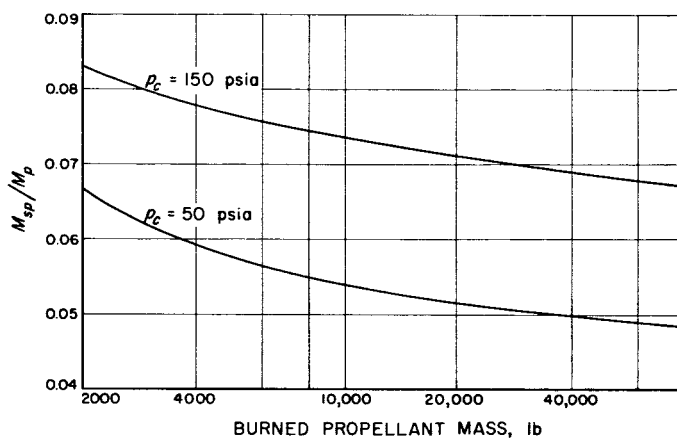$$M_{pa} = \left(\frac{M_s}{M_p}\right)M_p + \left(\frac{M_f}{F}\right)F$$

Figure 30. Propellant scaled system mass as a function of burned propellant load for a hydrazine–nitrogen tetroxide rocket system
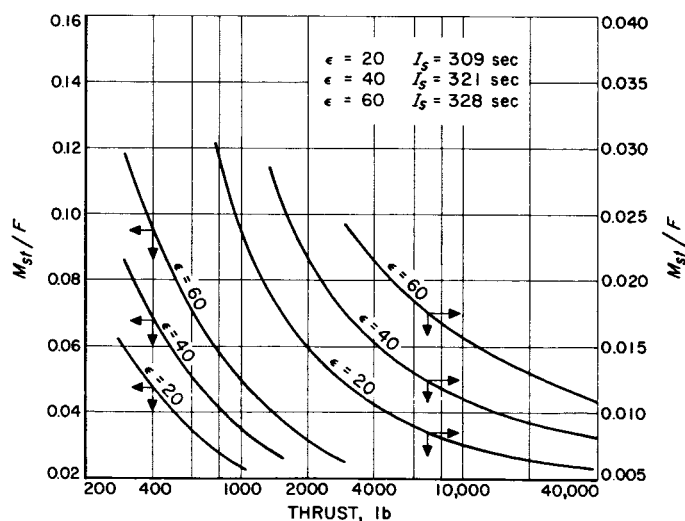

Figure 31. Thrust scaled system mass as a function of thrust level for $N_2H_4-N_2O_4$ system, using Pyrographite chamber at 50 psia

Using the performance estimates as determined in the preceding discussion, the propulsion system mass and gross payload mass have been computed for two Mars orbiter retro-missions. The gross mass selected for each of these spacecraft is 5000 pounds. A thrust level of
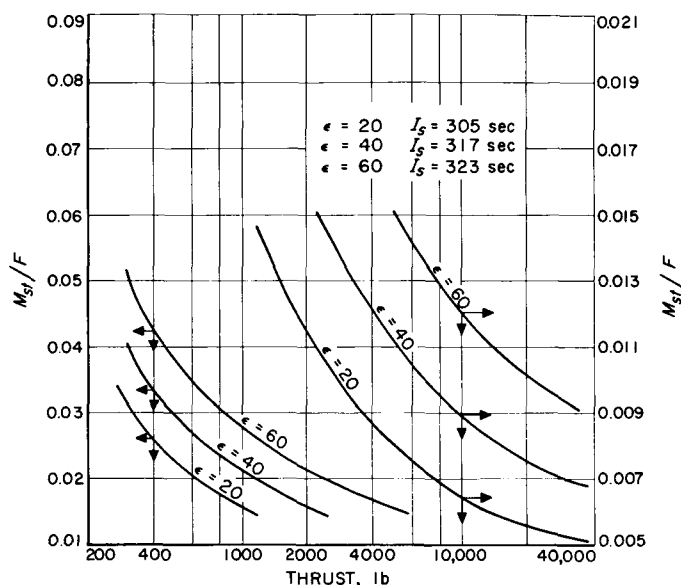

Figure 32. Thrust scaled system mass as a function of thrust level for N_2H_4–N_2O_4 system, using Pyrographite chamber at 150 psia
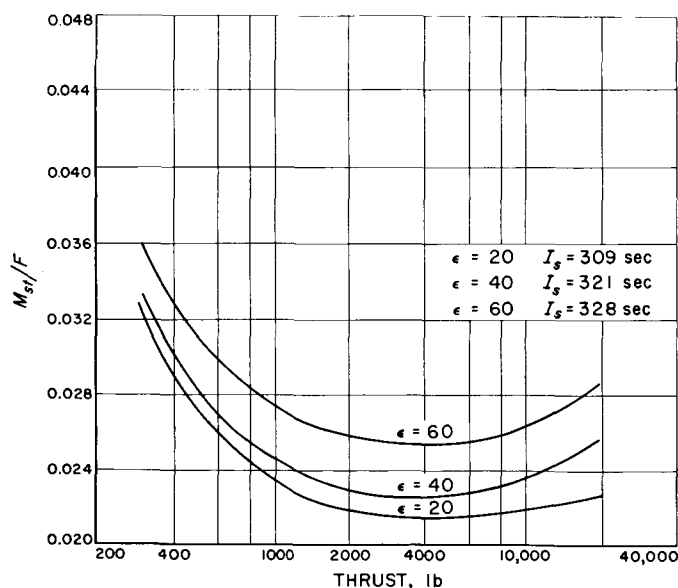

Figure 33. Thrust scaled system mass as a function of thrust level for N_2H_4–N_2O_4 system, using tungsten chamber at 50 psia
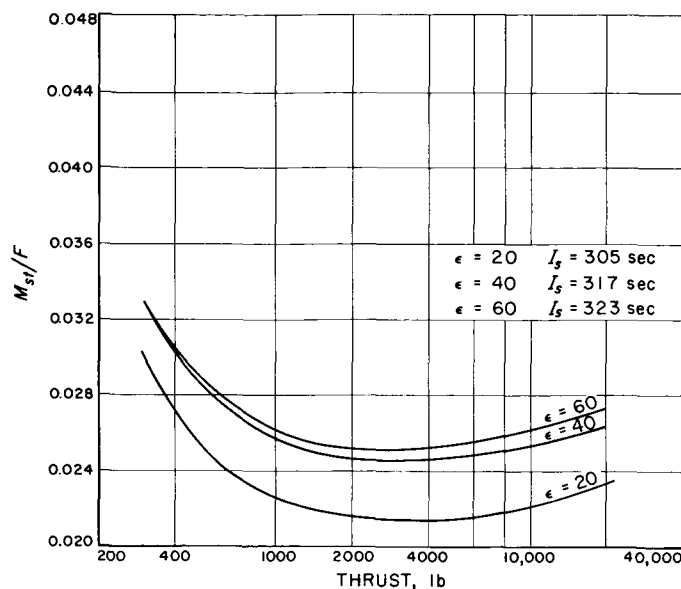

Figure 34. Thrust scaled system mass as a function of thrust level for N_2H_4–N_2O_4 system, using tungsten chamber at 150 psia

4000 pounds results in an initial vehicle acceleration of 0.8 Earth gravity and near-negligible potential losses.

Two orbits about Mars have been considered. The first is a 1000-mile apoapsis to 500-mile periapsis ellipse established after an approximately 180-day transit from Earth ($v_h = 19,600$). The other is a 500- to 10,000-mile ellipse established after a 240-day transit from Earth

Table 13. Mars orbiter payload comparison[a]

Chamber parameters			Payload mass, lb $(5000 - M_p - M_{ps})$	
p_c, psia	ϵ	Chamber material	High-energy orbit, $\Delta V = 14,500$ ft/sec	Low-energy orbit, $\Delta V = 7500$ ft/sec
50	20	Pyrolytic graphite	888	2140
50	40	Pyrolytic graphite	938	2184
50	60	Pyrolytic graphite	952	2202
150	20	Pyrolytic graphite	803	2069
150	40	Pyrolytic graphite	861	2132
150	60	Pyrolytic graphite	872	2145
50	20	Tungsten	844	2095
50	40	Tungsten	909	2155
50	60	Tungsten	937	2187
150	20	Tungsten	752	2018
150	40	Tungsten	811	2081
150	60	Tungsten	838	2111

[a]Gravity burning-time loss effects have been included.

($v_h = 14,750$). The impulsive velocity addition in the vicinity of the target is 14,500 and 7500 ft/sec, respectively. These particular missions were selected because they encompass the range of velocity demand which is consistent with currently anticipated communication distance constraints and scientific objectives.

Table 13 presents a payload mass comparison for these two missions, with the variations due to alternative chamber pressure and thrust chamber construction included. The gross payload mass varies from 752 to 952

pounds for the high-energy mission and from 2018 to 2202 pounds for the low-energy one. Table 14 contains a detailed inert system mass breakdown for an example retro-rocket; namely, the low-energy Mars-orbiting retro-propulsion system presented in Table 13. The configuration of this example stage is presented in Figure 35.

The results of this preliminary design study will be compared with those of other propulsion systems, both solid and liquid propellant, and presented in future _Research Summaries_.
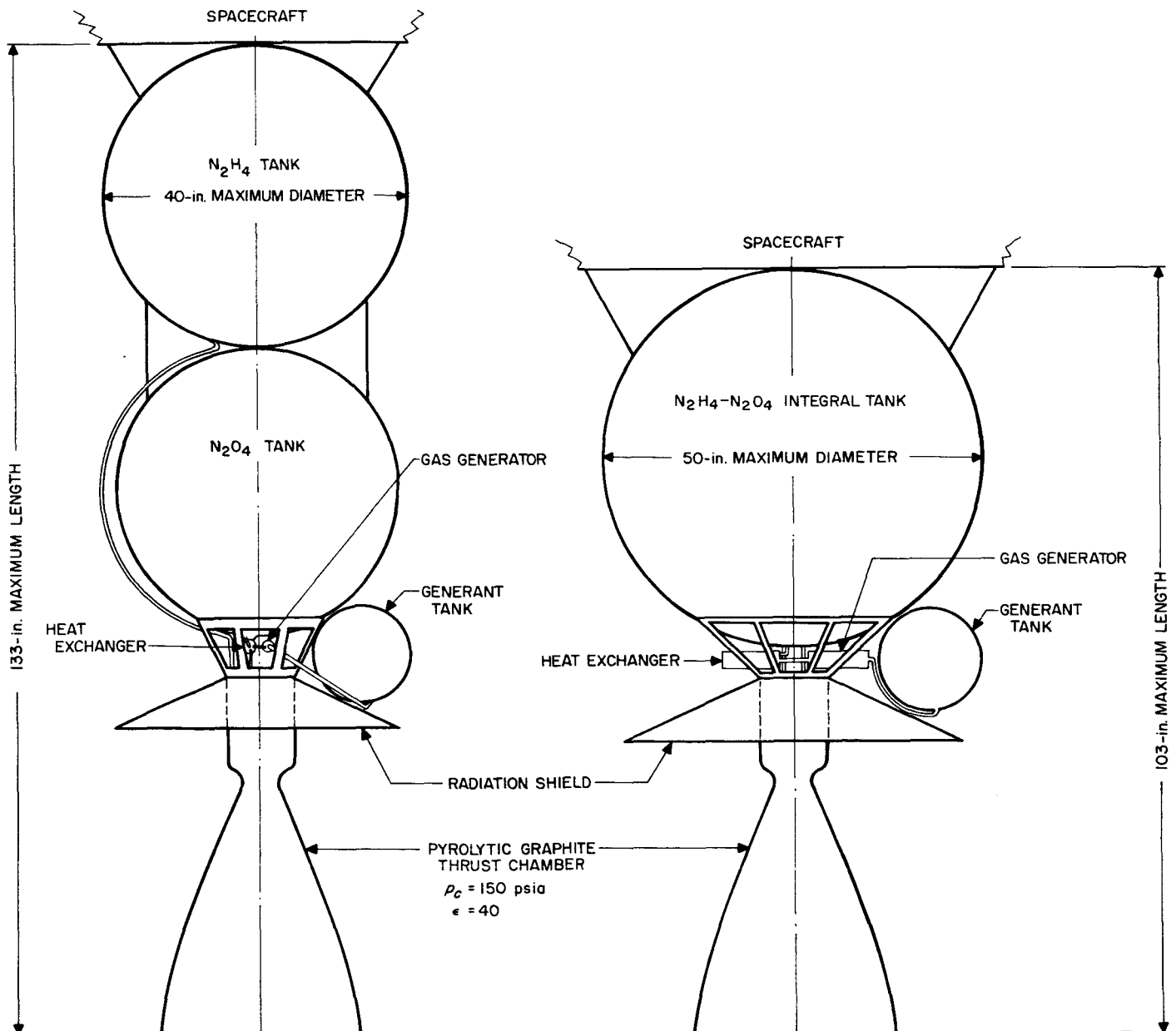

Figure 35. Possible configurations for retro-rocket

Table 14. Mass breakdown of example rocket

Item	Component	Mass, lb		Item	Component	Mass, lb
1	N_2H_4 tank (aluminum)	32.7		11	Lines	3.1
2	N_2O_4 tank (aluminum)	27.7		12	Propellant valve	3.3
3	Generant tank (aluminum, including He)	4.5		13	Injector	4.5
4	Generant (N_2H_4)	15.7		14	Thrust chamber (pyrolytic graphite)[a]	32.5
5	N_2H_4 bladder (Teflon)	4.8		15	Structure	38
6	N_2O_4 bladder (Teflon)	4.3		16	Radiation shield	3.8
7	Generant bladder (Teflon)	0.3		17	Holdup and reserves	52
8	Generant regulator	0.5		18	Contingency and brackets	23.2
9	Gas generator (including valve and start slug)	2.5		19	Control valve	0.7
10	Heat exchanger	4.5			Total propulsion system mass	258.6

[a] If the thrust chamber were tungsten, the total propulsion system mass would be about 310 pounds, or using a regeneratively cooled (fuel) thrust chamber, the total propulsion system mass would be about 289 pounds.

References

1. Barth, C. A., *Nitrogen and Oxygen Atomic Reactions in the Chemosphere*, Technical Report No. 32-63, Jet Propulsion Laboratory, Pasadena, March 24, 1961.

2. Hibbs, A. R. and Newburn, R., *Exploration of the Moon, the Planets, and Interplanetary Space*, Report No. 30-1, Jet Propulsion Laboratory, Pasadena, April 30, 1959.

3. Case, K. M., "Elementary Solutions of the Transport Equation and Their Applications," *Annals of Physics*, 9: 1–23, 1960.

4. Magnus, W. and Oberhettinger, F., *Formulas and Theorems for the Functions of Mathematical Physics*, Chelsea Publishing Co., New York, p 56, 1954.

5. Beatty, K. A., Armstrong, A. A., Jr., and Schoenborn, E. M., "Thermal Conductivity of Homogeneous Materials," *Industrial and Engineering Chemistry*, 42: 1527–1532, August 1950.

6. Plastics Properties Chart, *Modern Plastics Encyclopedia*, Part I, Hildreth Press, Inc., Bristol, Connecticut, September 1958.

7. Mixer, R. Y. and Marynowski, C. W., *A Study of the Mechanism of Ablation of Reinforced Plastics*, WADC TR 59-668, Part I, Wright Air Development Center, Dayton, October 1959.

8. Williams, H. E., *Axisymmetrical Shallow Loading of Thin, Spherical Shells*, Technical Report No. 32-48, Jet Propulsion Laboratory, Pasadena, February 7, 1961.

9. Williams, H. E., *The Effect of Rigid Inserts in Pressurized Spherical Shells*, Technical Report No. 32-49, Jet Propulsion Laboratory, Pasadena, February 14, 1961.

10. Williams, H. E., *Axisymmetrical Edge Loading of Shells of Revolution*, Technical Report No. 32-50, Jet Propulsion Laboratory, Pasadena, March 20, 1961.

11. Williams, H. E., *Influence Coefficients of Shallow Spherical Shells*, Technical Report No. 32-51, Jet Propulsion Laboratory, Pasadena, March 21, 1961.

12. Williams, H. E., *Axisymmetrical Pressure Loading of Thin Shells of Revolution—Approximate Membrane Solution*, Technical Report No. 32-52, Jet Propulsion Laboratory, Pasadena, March 22, 1961.

13. Williams, H. E., *Spherical Shells Supported at Isolated Points*, Technical Report No. 32-53, Jet Propulsion Laboratory, Pasadena, February 14, 1961.

14. Williams, H. E., *Analysis of a Circular Cylindrical Shell Loaded as a Cantilever*, Technical Report No. 32-64, Jet Propulsion Laboratory, Pasadena, March 15, 1961.

15. Kolb, A. C., "Magnetic Compression of Plasmas," *Reviews of Modern Physics*, 32 (No. 4), October 1960.

16. Cowling, T. G., *Magnetohydronamics*, Interscience Publishers, Inc., New York, 1957.

17. Van De Verg, N. and De Vorkin, H., *An Investigation of the Influence of Rocket-Chamber Configuration on Performance*, Progress Report No. 1-82, Jet Propulsion Laboratory, Pasadena, June 4, 1952.

18. Bartz, D. R., "A Simple Equation for Rapid Estimation of Rocket Nozzle Convective Heat Transfer Coefficients," *Jet Propulsion*, 27 (1): 49–51, January 1957.

19. Eckert, E. R. G., *Survey on Heat Transfer at High Speeds*, WADC TR 54-70, Wright Air Development Center, Dayton, April 1954.

20. Welsh, W. E. and Witte, A. B., *Comparison of Analytical and Experimental Local Heat Fluxes in Liquid Propellant Rocket Thrust Chambers*, Technical Release No. 34-114, Jet Propulsion Laboratory, Pasadena, November 14, 1960.